Analytical Models to Predict Power Harvesting with Piezoelectric Materials

By

Timothy Eggborn

Thesis submitted to the Faculty of the
Virginia Polytechnic Institute and State University
In partial fulfillment of the requirements for the degree of

Master of Science
In
Mechanical Engineering

Keywords: piezoelectric, analytical, model, beam, plate, cantilever, power, harvest

Daniel J. Inman, Chair
Donald J. Leo
Harry H. Robertshaw

May 2003
Blacksburg, Virginia

Analytical Models to Predict Power Harvesting with Piezoelectric Materials

Timothy Eggborn, M.S.
Virginia Polytechnic Institute and State University, 2003
Advisor: Daniel J. Inman

Abstract

With piezoceramic materials, it is possible to harvest power from vibrating structures. It has been proven that micro- to milliwatts of power can be generated from vibrating systems. We develop definitive, analytical models to predict the power generated from a cantilever beam and cantilever plate. Harmonic oscillations and random noise will be the two different forcing functions used to drive each system. The predictive models are validated by being compared to experimental data. A parametric study is also performed in an attempt to optimize the cantilever beam system's power generation capability.

To my father,
Hugh Eggborn,
And my mother,
Carol Eggborn

Acknowledgments

I would like to thank my advisor, Dr. Daniel J. Inman, for his guidance and patience throughout my graduate career at Virginia Polytechnic Institute and State University. I would also like to extend my thanks to Dr. Donald J. Leo and Dr. Harry H. Robertshaw as members of my advisory committee.

Additionally, I want to thank my colleagues in the Center for Intelligent Material Systems and Structures. I wish you the best in all your endeavors. A special thanks I would like to extend to R. Brett Williams, Ph.D. candidate, for his help throughout my research. Also, I would like to give my thanks to Dr. Gyuhae Park for his help at the beginning stages of my research.

Finally, I would like to thank my parents and family for their support and love throughout my college career.

Timothy Eggborn

Virginia Polytechnic Institute and State University
May 2003

Contents

List of Tables

List of Figures

Chapter 1

Introduction

In our world today, we are unmistakably moving towards a technological way of life. More and more people are carrying portable electronic devices than ever before. These devices allow for unbelievable power and versatility in communication and problem solving. But, as the technology for portables has grown tremendously, battery and energy storage technology has not kept up. New technology allows for these portables to become smaller, but battery size remains the same. Perhaps, sometimes the battery must be larger in order to accommodate the greater power demands by a portable device. An alternative for batteries is to create energy while on the go. Using piezoceramic materials is one way we can accomplish this. These “smart materials” can convert mechanical strain energy to electrical energy.

Research in the piezoceramic field generally concerns actuation and control or self-sensing technology. An up-and-coming field of research, is power harvesting with piezoelectric materials. In 1984, researchers implanted polyvinylidene fluoride (PVDF) patch onto the rib cage of a mongrel dog to harvest energy during inspiration (Hausler [1984]). Other experiments followed, and many were successful in harvesting several microwatts to milliwatts of usable power. One area in piezoceramic research that has been neglected is the modeling of piezoelectric generators on cantilever beams and plates, as well as the optimization of piezoceramic models in the use of power harvesting.

Several modeling techniques exist in which the piezoceramic is bonded to a structure. These models have different levels of difficulty and some take longer than others to accurately develop. If these models were compared to experimental data, the most accurate model could be determined. This most accurate model does not necessarily have to the most comprehensive. Once the best model is determined and to further optimize the power harvesting process, a parametric study could be performed in order to further optimize the power harvesting process.

This thesis will explore the theoretical values and predicted values of power and comparing them to experimental results. This thesis will also develop a reliable analytical model that predicts the experimental output power values so to bypass the lengthy process of fabricating a structure and test setup and performing time consuming measurements. A parametric study will also be conducted to further optimize the power harvesting process. In the next section, a literature review of power harvesting and applications of power harvesting is presented.

1.1 Literature Review

1.1.1 Piezo-based power generation

Umeda *et al.* (1996) sought after a device that would eliminate the need to charge up portables before taking them anywhere. The device would charge the mobile device enroute while traveling. To accomplish this, they constructed a piezo-generator that transforms mechanical impact energy to electrical energy by using a steel ball which impacts the generator. The steel ball is initially 5*mm* above a bronze disk (27*mm* in diameter and 0*.25mm* thick). The ball falls and strikes the center of the disk producing a bending vibration. The ball continues to bounce on the disk till it stops. The piezo patch converts the vibrational energy of the bouncing ball to electrical energy and stores a voltage in a capacitor. They performed analyses on two things. The first case was on the first impact. The second case was on multiple impacts from the ball. For the first case, higher voltage and capacitance affects the generator. A higher voltage decreases the time during which the current flows. If the capacitance is small, the voltage will go up quickly, limiting the time current will flow. On the other hand, if the capacitance is large, it takes time for the voltage to build up and allows the current to flow for more time. For the second case, the capacitance affects multiple impacts the same way it does for a single impact. As the initial voltage increases, the charge decreases for each capacitance. The achieved a maximum efficiency of 35% which is over three times higher than a solar cell.

In a following paper, Umeda *et al*. (1997) focus on the experiment done previously. They calculate that at dropping the ball from a height of *20mm*, the steel ball had 67.5% of its kinetic energy after the bounce. So, in order to harvest that unused energy, they conclude that the ball would need to stay in contact and not bounce off of the plate. A simulation of this gives a maximum efficiency of 52%. Keeping the ball from bouncing would be difficult and impractical, but internal inertia of the generator, if accelerated and stopped quickly, would be similar. They discover several things: the waveform of output voltage is changed by the load resistance, an optimum value exists for the load resistance which gives the maximum efficiency, much of the mechanical impact energy is transferred to the steel ball after the bounce as kinetic energy, the output energy to the load resistance will increase if the steel ball does not bounce off and vibrates with the transducer until the vibration stops. The efficiency increases if the mechanical quality factor increases, the electromechanical coupling coefficient increases and the dielectric loss decreases.

Amirtharajah (1997) writes a short, one page paper about a vibration based generator. They found that at 1000*Hz* the power was very low, while at 5*Hz* the power was high. Ideally, the resonant frequency should be close to the expected input frequencies. This is not always the case. Sometimes it is hard to design the generator to meet the specification. Even in the first case the DC power was approximately $800\mu m$. They built a DSP system which was low power. The generator consisted of a moving coil loudspeaker used as a microphone. The full system worked from 100*kHz* to 1*MHz* for an output voltage from about 0.85*V* to 0.97*V*.

Kasyap *et al.* (2002) vibrate a cantilever beam with a PZT patch attached in order to produce an electrical charge. The scientists harvested this vibrational energy and stored it using a flyback converter. They modeled the system using an LEM (lumped element model), which is an equivalent circuit of the system. Using the flyback converter and running the piezo at resonance, an efficiency of 20% is achieved.

Sodano *et al.* (2002) use a PSI-5h4e piezo bonded onto a plate $(80mm \times 40mm \times 0.095in.)$ to collect a charge in first, a capacitor, and second in a NiMH cell. For the capacitor, they use an adaptation of a circuit designed for a self-powered RF tag (Kymissis *et al.*, 1998). The vibration of a car compressor was modeled as a chirp signal from $0-250Hz$, and a shaker was used to excite the plate. Using two different configurations (one patch $62mm \times 40mm$, and three patches connected in series of the same area), they calculated average power and maximum power for four separate runs of the one plate configuration and one run of the three-plate configuration. They concluded that both the capacitor and NiMH cell could be used to store a charge from a vibrational source. Excluding an outlier test run, the average power for the one-plate configuration was $0.17mW$. If the outlier is taken under consideration the average power dips to $0.142mW$. The maximum power generated from the one-plate configuration was $1.92mW$. The average and maximum power from the three-plate configuration were $0.178mW$ and $1.8mW$, respectively.

With decreasing power requirements for sensors, Elvin et al. (2001) say that it seems feasible to harvest the power at the source and transmit the information wirelessly to a receiver elsewhere. A beam with an attached piezoceramic patch is modeled using the Rayleigh-Ritz method. A half-diode bridge is connected to a charging capacitor with a resistor across the capacitor to account for voltage leakage. An RF transmitter can be powered by the stored energy in the capacitor. The capacitor is allowed to charge up to $1.1V$, then discharged until $0.8V$ is reached. One charging/discharging cycle takes approximately one second.

Ottman (2002), *et al*, attempt to optimize the power transferred by a vibrating piezoelectric transducer to a battery. An AC-DC rectifier is attached to an equivalent circuit of a piezoelectric material since the piezoceramic produces an AC voltage and a battery needs a DC signal. A DC-DC converter is placed between the rectifier output and the battery. To achieve maximum battery current, the duty cycle was incrementally increased or decreased by a controller to change the current position on the current versus duty cycle curve. An algorithm is produced, and the adaptive controller is used to maintain the maximum power into the battery if the input is varied. The controller allows for the circuit to be used on many different vibrating structures. To power the controller and circuitry with vibrations, a larger array of piezoceramics must be used to generate the required power.

Hoffmann *et al.* (2002), want to improve upon the direct charging of a battery across the rectifier circuit. This method is non-optimal, and a converter would be able to optimize the charging process. The converter switching frequency was found to be 1*kHz*. This is where the harvested power peaked. The optimal duty cycle is also found experimentally. By using the step-down converter with the fixed duty cycle, the harvested energy was increased 325%.

Lesieutre, *et al* (2002), states that structural damping occurs when electrical energy is removed from a piezoelectric system. The loss factor is a function of the piezoelectric coupling coefficient. Damping increases directly as the coupling coefficient increases. The loss factor also depends on the ratio of the operating rectifier output voltage to the maximum open-circuit value. Energy harvesting added an additional damping percentage of 2.2%. Additionally, a stand-alone harvesting system was developed. For low excitation levels, a rectifier charges a battery directly. For high excitation levels, a DC-DC converter was used and results in more than four times the amount of power than without using the converter.

1.1.2 Piezo-based power generation applications

Hausler (1984) discusses implanting piezoceramic patches into a living body to harvest power from breathing, more specifically the elongation of the inspiration phase. The area where the patch might be located could be the lateral area of an upper rib. The power requirement for pulmonary ventilation is between 0.1 and 40*W*. So the 5*mW* needed to get 1*mW* with a 20% coupling coefficient is negligible. They used two PVDF with a 15% coupling coefficient and a max strain safety strain of 2%, weighing 128*mg*, and allowing a max power of $240\mu m$. These sheets are rolled into a tube with a 2.6*mm* diameter and length of 40*mm*. Simulating rub movements with an external mechanical arrangement, they measured an electric power of $20\mu W$. A mongrel dog weighing 25*kg* was operated on to attach the device. A voltage of 18*V* corresponded to a power of $17\mu W$. This power was constant for three hours until the experiment was terminated. The strain was only 0.5% instead of 2%. In conclusion, this power is too small. A film with 30% coupling coefficient and a mass of 100*mg* and an electric power output of 1*mW* should be more appropriate. Also, the alternating voltage would need to be rectified and stored in a Lithium accumulator.

Starner (1996) talks about how the human body stores a mass amount of energy. If scientists could tap into that reserve energy, batteries could be eliminated *per se*. Body heat, blood pressure, breath pressure, chest expansion from breathing, and upper limb movement all have potential but also have severe limitations. He came to the same conclusion as Gonzalez, walking has the most potential for energy conversion. Using piezoelectric materials such as PVDF in the soles of shoes can generate up to 5W from a small person (52kg) walking two steps per second. Storing the energy once it has been harvested is a project in and of itself. Capacitors drain about 50% of the power just from being charged up. He then goes on to discuss low power, functional computers that could be worn and made to use only 0.5W.

Kendall (1998) uses the Thunder PZT unimorph; the PZT is pre-stressed and mounted on a curved piece of steel. The PZT is attached into the heel of the shoe. A PVDF patch is positioned beneath the ball of the foot to provide maximum bending strain. Power output is as follows. For 2Hz, the PZT had peak voltages of 50V to peak power output of 15mW. The PVDF had peak voltage of 15V and a peak power of 2mW. The generator used produced a power output of 250mW with a RMS voltage of 1.8V across a 10Ω resistor (internal impedance). The generator is very cumbersome and the PVDF is the best because of its innocuousness. The Thunder PZT is more difficult to incorporate into the shoe because of its curved shape.

Kymissis *et al.* (1999) use three different apparatuses to "parasitically" collect energy which other words would be lost to the environment. More specifically, collecting power from the transfer of weight during a person's step. A sport sneaker was used as opposed to a hard soled shoe. The sneaker's sole absorbs some energy from hitting the ground while the person steps down. As the sole springs back while the foot is being lifted, the sole does not exert as much force as it did before, thus returning less energy. The difference in energy is what they are trying to collect. The first device used was to capture energy lost by the bending of the sole. Eight piezo films are stacked to form a bimorph PVDF. When the sole is bent these foils, which are connected in parallel, produce a net capacitance of 330nF. The second mode of harvesting lost energy is to collect energy exerted in heel strikes. A Thunder sensor/actuator was used. This PZT composite was bonded to a curved piece of steel. The heel strike pushes down on the top of the curved apparatus and presses it flat. The last technique used for collecting energy was a standard electromagnetic generator. When the heel strikes the ground, a lever cranks the rotary generator. It has a 3*cm* stroke. It produced two orders of magnitude more power than the piezoceramics but was much more cumbersome. Both the PZT and PVDF were easily integrated into the shoe and were hardly noticeable.

Gonzalez *et al.* (2000) discusses portable applications and the power requirements for each device. Low intensity power requirements for communication devices such as Bluetooth and GSM range between 12–18*mW*. Sources of mechanical energy in the human body are then described. Breath and blood pressure are possible but not practical for use in energy conversion to electrical energy. Upper arm and finger movements prove to be too sporadic to provide continuous power. Expansion of the rib cage during exhalation could be used in the future to harvest energy. PZT patches attached to a ring which fits around the rib cage would strain during exhalation and produce a voltage. The total electrical energy available from exhalation is calculated to be 0.4*W*. Walking appears to be the best choice, offering 67*W* of total mechanical energy generated with a range of 5–8.4*W* available for electrical power.

Allen (2001) develops an energy harvesting eel, a piezoelectric membrane that is placed in the wake of a bluff body. Oscillations will occur in the membrane and produce a charge in the membrane due to external forcing by vortex shedding downstream. This charge could be used to trickle-charge a battery in a remote location.

1.1.3 Non-piezo-based power generation

Lakic (1989) makes an airbag that can be adjusted for snugness in a ski boot. The foot warmer mechanism is mounted entirely on an insert for the outer boot or shoe, and includes an electrical resistance heater, an electrical generator, a mechanical transducer to translate vertical movements of the wearer's heel into uni-directional rotational movement of a flywheel, and a gear box mechanically coupling the flywheel to the electrical generator. Specific features of the invention include an air pump to supply air pressure to an air chamber, including an air bag which extends over the instep of the shoe to control the snugness of the shoe; and communicating channels within the shoe to direct air across the electrical generator and heater and to the air bag, thereby warming the entire foot of the wearer. Further embodiments include tubing to direct warmed air to a suit having an inflated lining to warm the suit.

Amirtharajah (1998) develops a moving coil electromagnetic transducer that is used as a power generator. Up to $400\mu W$ can be generated. A chip was designed that will show a digital system operating on power generated from vibrations in the environment. The chip has an ultra-low power controller that uses delay feedback to control voltages. It also has a low power subband filter DSP load circuit. The system uses $18\mu W$ of power.

1.1.4 Modeling of Piezoelectrics on Beams and Plates

Crawley and de Luis (1986) develop analytical models of mechanical coupling between piezoelectric actuators and substrates. Static models are established to couple structures to several different actuator configurations, including surface-bonded and embedded configurations. These static models are then coupled into a dynamic model of a cantilever beam. They use the Rayleigh-Ritz equation of motion to model the beam. A scaling analysis is also performed to determine how changes in the structure affect the actuator efficiency. Also within the scaling analysis, Crawley and de Luis determined that taking the second derivative of the structure mode shapes and finding the resulting roots ("zero crossing points") represented "strain nodes." These "strain nodes" are points along the beam where the strain changes from positive to negative. Piezoelectrics should not be bonded across these "strain nodes" in order to maximize their effectiveness.

Kulkarni and Hanagud (1991) perform Tiersten's variational formulation and extend it to a generic three dimensional case. Formulations for small and large deflections are developed. Afterwards, a static analysis of two piezoelectric patches attached to a cantilever beam is performed. The electric field along the length of the actuators is varied. The analysis substantiates the existence of a two/three dimensional nature of the state of stress near the actuator tip. A dynamic analysis is also performed with several different loading cases. A sharp variation in shear stress is present with all the loading cases.

Dimitriadis *et al.* (1991) develop a theory for the excitation of two-dimensional thin elastic structures by piezoelectric patch actuators. This theory is applied to a simply supported rectangular thin plate by piezoelectric patches bonded symmetrically on both sides of the plate. By driving the actuators at the plate's resonant frequencies, it is possible to excite the individual plate modes. The modal response is directly related to the excitation frequency, patch shape, and patch location. Because of some evidence that the nodal lines are forced to the plate's simply supported boundaries, it may be implied that optimum actuator boundaries are along modal lines or at clamped edges when certain modes are excited.

Heyliger (1997) develops exact three-dimensional solutions for a laminated piezoelectric continuum. Exact in-plane Ritz method solutions are developed for free-vibration for piezoelectric plates in simply supported conditions. Multiple single layer theories, along with generalized theories are used to predict deflection and electric potential on several different cases of laminated thin and thick plates. The thick plates are piece-wise nonlinear, and only the generalized coupled theories provide adequate results. For predicting normal stress within the piezoelectric thin-layered plate, the generalized theories are capable to accurately evaluate the stress provided the number of layers does not exceed 25. Shear stress, which is the main cause of delamination of piezoelectric layers, is harder to predict. Point-wise integration of the stess-equilibrium equations is suggested to calculate a better estimate.

Wang *et al.* (1997) develops sets of equations for determining the deformation compatibility between piezoelectric patches and beams or plates. The interaction forces between the piezoelectric patches and substrates are caused by structural deformation and an electric field imposed upon the piezoelectric patch. The static capacitance is found to vary according to deformations caused by the imposing electric field. The piezoelectric patches could be used as sensors to monitor the change in static capacitance. With the same piezoelectric patches used as actuators, Wang *et al.* investigates actively controlling the substrate deformation by predicting the imposed voltage needed to restore the substrate to its original state.

He *et al.* (1998) develop a uniformizing approach to solving for free vibration analysis of simply-supported, composite plates. They develop equations for the mid-plane thickness, bending stiffness, and Poisson's ratio that would allow for simplifications to be made to a metal-piezoelectric composite thin plate. Boundary conditions for the composite plate are found to be the same as a single layered thin plate. By calculating new values for the variables listed above, He *et al.* establish an equivalent single layer plate. They validate the uniformizing method by comparing the natural frequencies to experimental natural frequencies.

Gao *et al.* (1998) perform a three dimensional analysis for free vibration on composite laminate plates with piezoelectric layers. Power series are used as solutions to displacement and electric potential. Analytical natural frequencies and mode shapes are calculated and compared to measured values. The power series expansion method is proven to be simple and convenient.

Liu *et al.* (1999) develop a finite element model based on classical laminate plate theory to determine shape control and active vibration suppression of composite plates with integrated piezoelectric actuators and sensors. Hamilton's principle is used to derive the dynamic equations of motion for the piezoelectric actuators and sensors. For sensors, the closed circuit charge is calculated by integrating all of the point charges on the sensor layer. The current on the surface of a sensor layer is defined as the derivative of charge with respect to time. The open circuit voltage can be calculated by multiplying the current by the gain of a current amplifier. Two cases are studied. The first is a piezoelectric cantilever beam consisting of two identical layers of piezofilm. The applied actuator voltage is measured between 0-500V and compared to the model's results. The second is shape and vibration control of a laminated plate using the finite element method.

1.2 Overview of Thesis

1.2.1 Research Objectives

The objective of this thesis is to find a more precise and predictive model of power harvesting. Multiple methods of modeling piezoceramics will be used in conjunction with beam and plate models to generate values of power produced from vibrational energy. Once these models are constructed, experimental results will be compared to each, resulting in a measure of accuracy. This measure of analytical accuracy will save time and money by avoiding performing multiple experiments.

1.2.2 Research Contributions

In this thesis a beam model and plate model are constructed, and power values extracted. What distinguishes this thesis from other literature is that the analytical power values were compared to experimental data in order to determine the most suitable predictive method for estimating power from vibrational systems. In addition, a parametric study is performed on the piezoceramic to further optimize the power harvesting process.

1.2.3 Approach

Chapter 2 is committed to discussing the analytical development of piezo-based power harvesting systems. Background information, including properties and governing equations is provided for lead-zirconate-titanate (PZT) piezoceramics. The PZT can be modeled a couple of ways. Three methods: the pin-force model, enhanced pin-force model, Euler-Bernoulli, and Energy method model will be discussed. Once the PZT has been adequately modeled, the beam and plate models will be constructed. . From these equations, voltage and, finally the power can be calculated.

Chapter 3 presents the parametric study of different PZT properties. The effects of PZT effective area and location on the beam will be investigated. The thickness of the beam and how it affects power generation will be investigated. Also, optimal force location will be discussed

Chapter 4 starts with the experimental procedures. The analytical models are compared to the experimental data. Possible explanations for variations in values of power from the experiment are explained.

Chapter 5 summarizes findings and conclusions, and proposes future works.

Chapter 2

Analytical estimation of power generation from a PZT

2.1 Introduction

This chapter deals with the development of the PZT models and the analytical estimations of power generation. Background information is given for the governing equations of piezoceramic sensors as well as for relationships between voltage and displacement and current and displacement. Each modeling technique used for PZTs will be discussed and constructed. Then, a cantilever beam with an external force applied will be analyzed analytically and the resultant power extracted. A cantilever plate model will also be made, and the power generated from the vibrational energy of an external force calculated as well.

2.2 Modeling of a piezoelectric bender sensor

This section provides background on piezoelectric bender sensors.

2.2.1 Background

Definition

In 1880, the Curie brothers, Pierre and Jacque, discovered the first incidence of piezoelectricity. Subjecting different substances to mechanical stress, the Curies discovered that certain ones such as Rochelle salt produced a resulting electrical charge. Lippmann predicted and the Curies later verified that the converse effect held true in

1881. Piezoelectric materials will exhibit a mechanical strain when a voltage is supplied to it. Hankel coined the term ‘piezoelectricity’ which is derived from the Greek word for ‘press’ (Ikeda [1996]).

Properties of Piezoelectric Materials

The most common types of piezoelectric materials are Lead Zirconate-Titanates (PZTs). PZTs are solid solutions of lead zirconate and lead titanate. These manufactured ceramics have much better properties than the naturally occurring piezoelectrics. Manufacturing PZTs takes multiple steps. First, raw materials are mixed together at a temperature of 800-1000 degrees C. A perovskite powder is formed and mixed with a binding agent. This mixture is then sintered into a desired shape. When cooled, the PZT unit cells take on a tetragonal structure with mechanical and electrical asymmetry (Sirohi [2000]). A unit cell in a raw PZT is shown in Figure 2.1-(1).

Poling is necessary for the material to take on piezoelectric properties. Poling is heating the material over the Curie Temperature which allows the molecules to move more freely and applying a large electric field which causes the crystals inside the material to align themselves in one direction (Figure 2.2-(2)). This phenomenon continues even after the electric field is taken off and the material cools (Figure 2.2-(3)). Figure 2.1-(2) shows the poling within the unit cell structure. The geometry of the unit cell becomes asymmetrical. Before poling, all the crystals within the material are positioned randomly and thus void of any piezoelectric characteristics. Now, when the material is compressed, a voltage with the same polarity as the poling voltage will appear across the electrodes. If the material is forced into tension, an opposite voltage will be produced across the electrodes. This is called the direct piezoelectric effect.

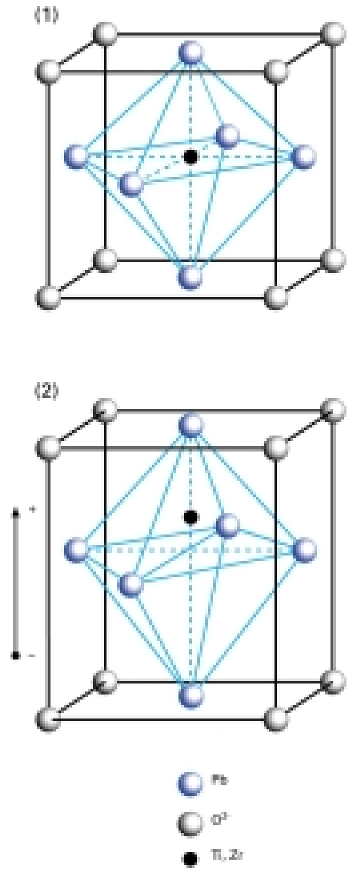

Figure 2.1. PZT unit cell: (1) before poling, (2) after poling (Physik Instrumente [2002])

2.2.2 PZT bender sensors

A PZT bender sensor is a thin wafer of PT material. To achieve a more useful bender, two thin wafers are adhered together and connected in parallel. PZT benders produce an electric field and thus a voltage in the 1-direction when subjected to transverse deflections caused by bending force strains in the 3-direction.

Modeling the bender as a sensor

Identifying the material, sub- and superscripts are used for each property coefficient. Sub-scripts are used as the orthogonal coordinate system to describe the PZT. Numbers 1, 2, and 3 refer to the principal axes, while 4, 5, and 6 refer to the shear effects around 1, 2, and 3, respectively. It is usually the case that poling is in the negative '3' direction.

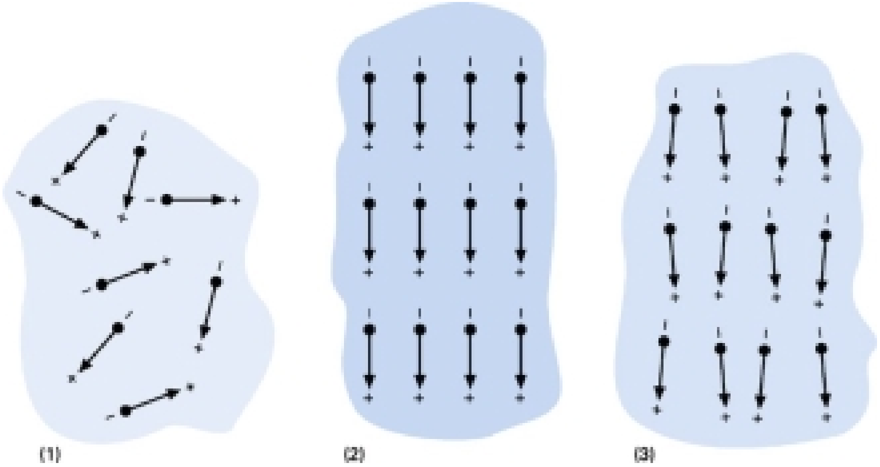

Figure 2.2. Electric dipoles in domains: (1) unpoled ferroelectric ceramic, (2) during and (3) after poling (Physik Instrumente [2002])

Usually, the piezoelectric constants have double sub-scripts. The first sub-script corresponds to the direction in which an electrical field is produced on the material. The second sub-script denotes the direction of the mechanical strain that the material experiences. Figure 2.3 shows orthogonal coordinate system and the poling direction.

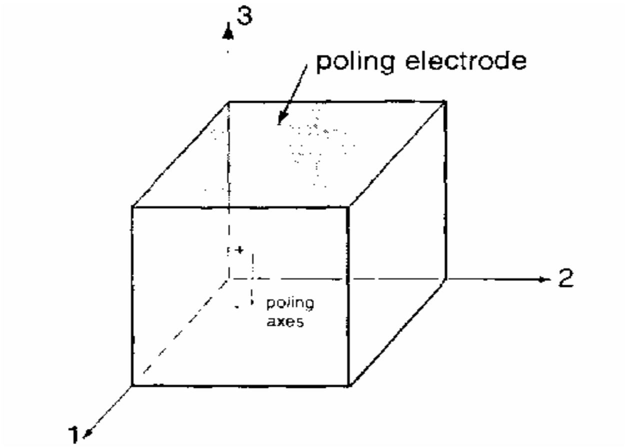

Figure 2.3. Orthogonal coordinate system and poling direction that is used in this thesis (Inman [1996]).

For the piezoelectric bender, the constitutive equations are as follows (ANSI/IEEE [1987]):

$$\varepsilon_1 = s_{11}^{E}\sigma_1 + d_{13}E_3 \qquad (2.1)$$

$$D_3 = d_{31}\sigma_1 + e_{33}^{T}E_3 \qquad (2.2)$$

where,

ε = Mechanical Strain $\left(\frac{m}{m}\right)$

σ = Mechanical Stress $\left(\frac{N}{m^2}\right)$

E = Electrical Field $\left(\frac{\mathrm{V}}{m}\right)$

D = Electric Density $\left(\frac{C}{m^2}\right)$

s = Elastic Compliance $\left(\frac{m^2}{N}\right)$

d = Piezoelectric Strain Coeff. $\left(\frac{m}{V}\right)$

e = Electric Permittivity $\left(\frac{F}{m}\right)$

Boundary conditions are denoted by super-scripts. The four boundary conditions that are used are:

T = constant stress (mechanically free)
S = constant strain (mechanically constrained)
D = constant electrical displacement (open circuit)
E = constant field (short circuit).

2.3 Mathematical modeling of a unimorph beam sensor

Modeling of a unimorph beam, or a beam with a single wafer mounted on its surface, is presented in this section. The three most common methods will be discussed.

The pin-force model is the most primitive of the three methods. The enhanced-pin force model expands upon the pin-force concept. The Euler-Bernoulli model is the most complex of the three.

2.3.1 Modeling the PZT sensor using the Pin-Force method

The pin-force model describes the mechanical interaction between the piezoelectric and the substrate elements. Pins connect the two elements at the extreme ends of the PZT. Perfect bonding between the two elements is implied, and the adhesive layer is infinitely stiff. Accuracy is decreased, however, as the adhesive layer becomes thicker, or the bonding material becomes less stiff. Shear stress in the piezoelectric is concentrated only in a small area at the pin ends. The strain in the beam is assumed to follow Euler-Bernoulli beam theory where the strain increases linearly through the thickness. Though in the piezoceramic, the strain is assumed to be constant through the thickness. Because of this constant strain, the pin-force method does not take into consideration the bending stiffness of the piezoelectric patches, and the method is limited when the stiffness of the substrate becomes approximately five times larger than the piezo stiffness. Figure 2.4 shows the pin-force model strain state for a unimorph bender (Inman [1996]).

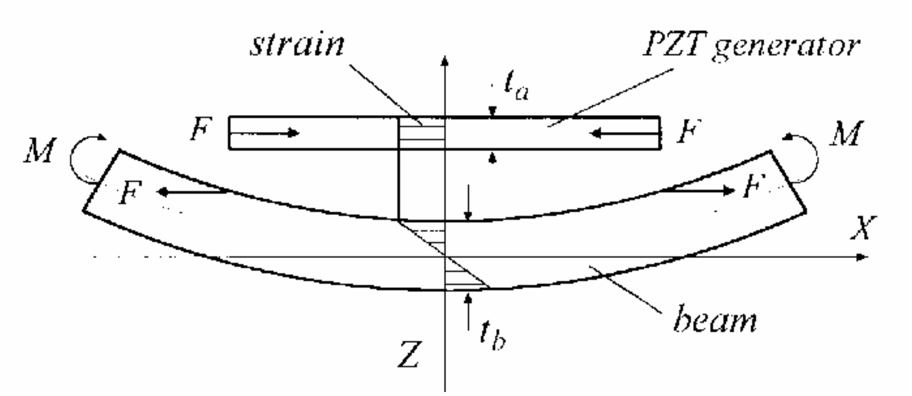

Figure 2.4. Pin-force model of unimorph PZT and substrate (Wang, K. [2001]).

Modeling the PZT as a generator (sensor) begins by first setting the convention for positive and negative moments acting on a beam. Figure 2.5 defines positive and negative moments.

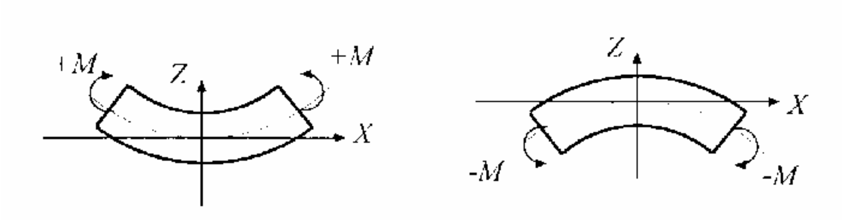

Figure 2.5. Notation of moments (Wang, K. [2001]).

The PZT is attached to the top of a thin beam. When the substrate and piezoelectric material are subjected to an external moment, the PZT strain ε_a can be written as

$$\varepsilon_a = \frac{\sigma_a}{E_a} \tag{2.3}$$

where σ_a is the PZT stress. Equation (2.3) can be rewritten as

$$\varepsilon_a = \frac{F}{E_a b t_a} \tag{2.4}$$

where F is the resultant force acting on the PZT caused by the moment. The strain on the beam is modeled as

$$\varepsilon_b = -\frac{t_b}{2}\kappa \tag{2.5}$$

where t_b is the beam thickness, and κ is the beam curvature. The strain acting on the PZT and the beam is the same; therefore, Equations (2.4 and 2.5) are equal ($\varepsilon_a = \varepsilon_b$).

The equation for the external moment applied to the beam is

$$M_b = M - F\frac{t_b}{2} = (E_b I_b)\kappa \tag{2.6}$$

where I_b is the moment area of inertia of the beam. Substituting Equation (2.4) into (2.5) gives an expression for curvature

$$\kappa = -\frac{2F}{E_a b t_a t_b} \tag{2.7}$$

Substituting Equation (2.7) into (2.6) gives

$$F = \frac{6E_a t_a M}{3E_a t_a t_b - E_b t_b{}^2} \tag{2.8}$$

Combining Equations (2.4) and (2.8) leads to a strain expression on the interface as

$$\varepsilon_p = \frac{6M}{b\left(3E_a t_a t_b - E_b t_b{}^2\right)} \tag{2.9}$$

The stress is $\sigma_a = E_a \varepsilon_a$ which gives

$$\sigma_a = \frac{6E_a M}{b\left(3E_a t_a t_b - E_b t_b{}^2\right)} \tag{2.10}$$

The voltage on the PZT poling surfaces is related to the stress by

$$V = g_{31} t_a \sigma_a \tag{2.11}$$

where g_{31} is the PZT voltage constant. The voltage is related to the moment by substituting Equation (2.10) into (2.11) as

$$V = \frac{6g_{31}M}{bt_b(3-\Psi)} \tag{2.12}$$

where $\Psi = \frac{E_b t_b}{E_a t_a}$ (Wang, K. [2001]).

2.3.2 Modeling the PZT sensor using the Enhanced Pin-Force mrthod

The enhanced pin-force model expands upon the pin-force model by taking under consideration the PZT bending stiffness. The strain does not remain constant as in the pin-force model but increases linearly through the PZT thickness. Figure 2.6 shows the diagram of the enhanced pin-force model. A drawback still exists when using this method: the PZT is assumed to bend on its own neutral axis. This assumption basically treats the PZT and substrate as two separate structures connected only by the end pins.

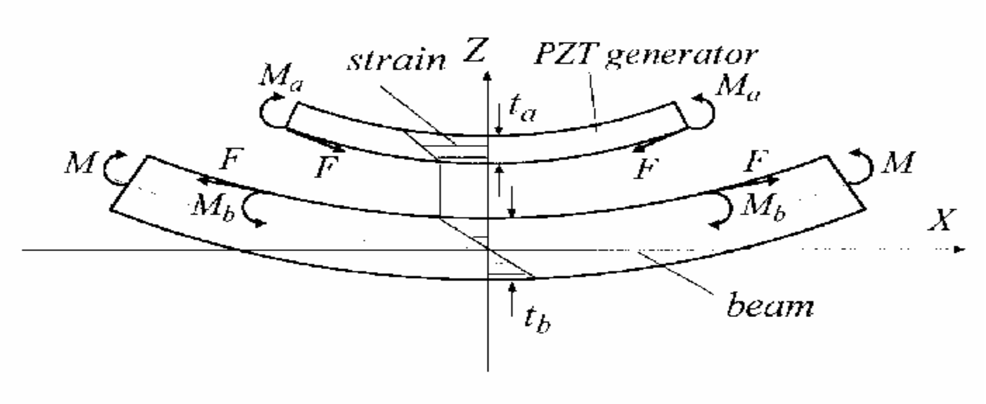

Figure 2.6. Enhanced pin-force model of unimorph PZT and substrate. (Wang, K. [2001]).

The moment acting on the beam is now

$$M_b = M - F\frac{t_b}{2} - M_b = (E_b I_b)\kappa \tag{2.13}$$

where $M_b = M_a = (E_a I_a)\kappa$. From Equations (2.4) and (2.5), an expression for the force F is

$$F = -\frac{E_a b t_a t_b}{2}\kappa \tag{2.14}$$

Combining Equations (2.13) and (2.14) gives the curvature as

$$\kappa = \frac{12M}{-6E_a b t_a t_b{}^2 + E_a b t_a{}^3 + E_b b t_b{}^3} \tag{2.15}$$

Substituting Equation (2.15) into (2.14) and then into (2.4) gives an expression for strain as

$$\varepsilon_a = \frac{6t_b M}{6E_a b t_a t_b{}^2 - E_a b t_a{}^3 - E_b b t_b{}^3} \tag{2.16}$$

The stress for the enhanced pin-force model will now be

$$\sigma_a = \frac{6E_a t_b M}{3E_a b t_a t_b{}^2 - E_a b t_a{}^3 - E_b b t_b{}^3} \tag{2.17}$$

Finally, substituting Equation (2.17) into (2.11) leads to

$$V = \frac{6g_{31}TM}{bt_a(3T^2 - 1 - \Psi T^2)} \tag{2.18}$$

where $T = \dfrac{t_b}{t_a}$.

2.3.3 Modeling the PZT sensor using the Euler Bernoulli method

The Euler-Bernoulli model is shown in Figure 2.7. Of the three models described, the Euler-Bernoulli model is the most accurate. The PZT and substrate both bend about a common neutral axis which is no longer the neutral axis of the beam. Perfect bonding is assumed, and the PZT is considered to be a layer of the beam. This neutral axis is calculated by a modulus-weighted algorithm. Figure 2.7 also shows the modulus-weighted cross section of the piezoelectric and substrate.

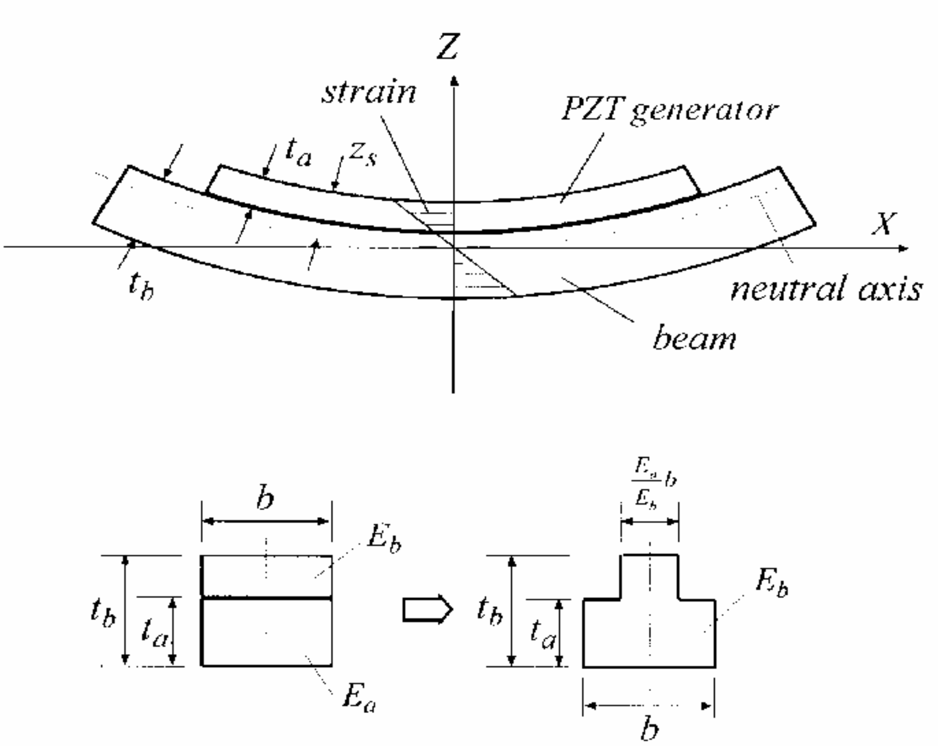

Figure 2.7. Euler Bernoulli model of PZT and substrate along with the modulus-weighted neutral axis. (Wang, K. [2001]).

The equation for the distance to the neutral axis can be written as

$$z_s = \frac{\sum_{i=1}^{n} z_i \frac{E_i}{E_r} A_i}{\sum_{i=1}^{n} \frac{E_i}{E_r} A_i} = \frac{\frac{t_a}{2} t_a \frac{E_a}{E_b} + \left(t_a + \frac{t_b}{2} \right) t_b}{t_a \frac{E_a}{E_b} + t_b} \tag{2.19}$$

To simplify the calculations, the average strain in the PZT is determined and used to find the voltage. The average strain is

$$\varepsilon_a = -\frac{M}{(E_a I_a + E_b I_b)} \left(z_s - \frac{t_a}{2} \right) \tag{2.20}$$

where

$$I_a = \int_{z_s - t_a}^{z_s} b z^2 dz = \frac{1}{3} b \left[z_s^{\ 3} - (z_s - t_a)^3 \right] \tag{2.21}$$

$$I_b = \int_{-(t_a + t_b - z_s)}^{z_s - t_a} b z^2 dz = \frac{1}{3} b \left[(t_a + t_b - z_s)^3 + (z_s - t_a)^3 \right] \tag{2.22}$$

Substituting Equation (2.19) into (2.20) gives

$$\varepsilon_a = -\frac{6 M E_b t_b (t_a + t_b)}{b[E_a^{\ 2} t_a^{\ 4} + E_b^{\ 2} t_b^{\ 4} + 2 E_a t_a E_b t_b (2 t_a^{\ 2} + 3 t_a t_b + 2 t_b^{\ 2})]} \tag{2.23}$$

Finally, substituting Equation (2.23) into $\sigma_a = E_a \varepsilon_a$ and then into (2.11) leads to the voltage as

$$V = -\frac{6 g_{31} M \Psi (1 + T)}{b t_a [1 + \Psi^2 T^2 + 2\Psi (2 + 3T + 2T^2)]} \qquad (2.24).$$

2.4 PZT generator as a circuit

The piezoelectric material can be described using an electrical model shown in Figure 2.8. Piezoelectric materials have internal impedances which will dissipate energy. Some power will be lost when generated by the PZT because of this effect. Impedance matching which maximizes power output will also be discussed.

As a generator, the PZT is an AC voltage source with an internal impedance. This internal impedance is found by using an HP 4192A Impedance Analyzer. The internal impedance is inversely proportional to frequency. The beam's internal impedance is measured as $330{,}000\Omega$ with a phase shift of -90 degrees at the first resonant frequency, $10.6Hz$. The resonant frequencies of the beam are calculated in the next section. The measured phase shift is present due to the capacitive nature of the PZT. The assumption is made, however, that the impedance is purely resistive and the imaginary value of impedance is ignored. This is a valid assumption because the resistive value is much larger than the capacitive value which can be calculated using the PZT properties in equation (2.25) given by

$$C_p = \frac{d_{31} L_p b}{g_{31} t_a} \tag{2.25}$$

where, L_p is the PZT length.

Matching the external load impedance with the internal PZT impedance will assure maximum power output. A relationship between power and resistance can be derived for a purely resistive circuit which is given by (Rizzoni [2001])

$$P = \frac{\tilde{V}_S^{\,2} R_L}{\left(R_S + R_L\right)^2} \tag{2.26}$$

where, $\tilde{V}_S$ is the RMS source voltage value in phasor notation, R_L and R_S are the resistance values for the load and source, respectively. It is evident that the maximum power is produced when $R_L = R_S$.

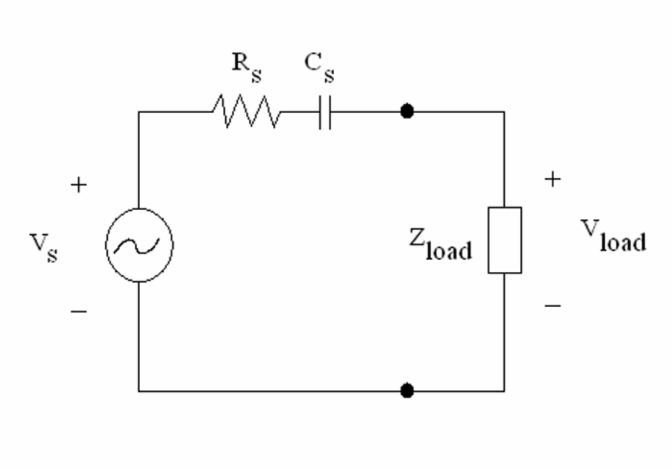

Figure 2.8. PZT generator circuit model.

2.5 Analytical power estimation

In this section, power harvesting results of a PZT will be calculated analytically. The substrate will first be modeled as a cantilever beam. The three modeling techniques of the PZT will be used and their results compared. Next, a clamped-free-free-free plate will be used as the substrate, and the three modeling techniques used and their results compared.

Two different driving functions will be applied to both the cantilever beam and clamped plate. A point-force, harmonic function will be applied to the PZT-substrate system. With a driving frequency close to the first resonant frequency of the substrate, the harmonic function will produce maximum displacement.

Not many applications experience vibrations that occur at their resonant frequencies only. Power harvesting devices would be more likely to exist in environments where they would be exposed to a wide range of vibrational frequencies. One such example is an air conditioner compressor found on a typical automobile. After the vibrations were measured, it was determined that the vibrations were random. For this reason, the second driving function will be a random noise generator which will simulate the random vibrations that were measured on the air conditioner compressor of an automobile.

2.5.1 Analytical power estimation: cantilever beam model

Figure 2.9 shows the setup for the cantilever beam model and Table 2.2 gives the beam and PZT dimensions and properties. Following the Euler Bernoulli definition of a beam, the length is over ten times larger than the width. The PZT is attached to the beam near the clamped edge for maximum strain. For the estimated power that a PZT can produce from beam vibrations to be calculated, the moment that the PZT experiences must first be determined. This moment can be evaluated by solving for the deflection of the beam and then estimating the experienced moment as a function of the beam's curvature.

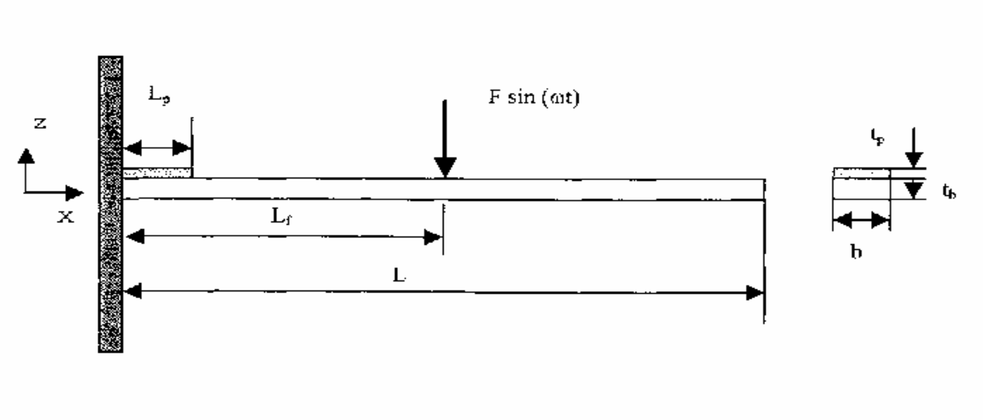

Figure 2.9. Setup of cantilever beam model.

Table 2.1. Dimensions and properties of the beam and PZT, respectively.

	Parameter	*Value*	*Units*
Beam	length	0.558	m
	width	0.050	m
	thickness	0.004	m
	density	2715	kg/m^3
	Young's Modulus	71×10^9	Pa
PZT	length	0.073	m
	width	0.050	m
	thickness	0.508	m
	Young's Modulus	62×10^9	Pa
	dielectric constant	-320×10^{-12}	m/V
	voltage constant	-9.5×10^{-3}	Vm/N
	internal resistance	330000	Ω

The Euler-Bernoulli method is used to model the cantilever beam. The governing equation of the beam is

$$\rho A\frac{\partial^4 w(x,t)}{\partial t^4}+E_b I_b\frac{\partial^4 w(x,t)}{\partial x^4}=F(t) \tag{2.27}$$

where w is the displacement of the beam, ρ is the density of the aluminum beam, A is the cross-sectional area, and $F(t)$ is the external force applied to the beam.

Beam with a Harmonic Driving Force

For this case, the beam is driven harmonically:

$$\frac{\partial^4 w(x,t)}{\partial t^4} + c^2 \frac{\partial^4 w(x,t)}{\partial x^4} = \frac{F_0}{\rho A}\sin(\omega t)\delta(x - L_f) \qquad (2.28)$$

where ω is the driving frequency, $c^2 = \frac{E_b I_b}{\rho A}$, and L_f is the position of the applied force from the clamped edge of the beam. The driving frequency will be equal to the beam's first natural frequency because the largest deflections occur at the first natural frequency.

The solution will take the form

$$w(x,t) = \sum_{i=1}^{3} q_i(t) X_i(x) \qquad (2.29)$$

where q_i is the *i*-th modal coordinate equation of the beam and X_i is the *i*-th mode shape of the beam. For consistency, only the first three mode shapes will be used. The general mode shape equation for a cantilever beam is found in Inman (2000) and is

$$X_i(x) = \cosh(\beta_i x) - \cos(\beta_i x) - \frac{\sinh(\beta_i L_b) - \sin(\beta_i L_b)}{\cosh(\beta_i L_b) + \cos(\beta_i L_b)}(\sinh(\beta_i x) - \sin(\beta_i x)) \qquad (2.30)$$

where L_b is the beam length, $\beta_i^4 = \frac{\omega_{ni}^2}{c^2}$ and ω_{ni}, the *i*-th natural frequency, is found from the characteristic equation

$$\cos(\beta_i L_b)\cosh(\beta_i L_b) = -1 \qquad (2.31).$$

Table 2.2 shows the first five natural frequencies.

Table 2.2. Beam natural frequencies.

Natural frequency	*rad/s*	*Hz*
1	66.68	10.612
2	417.87	66.506
3	1170.1	186.22
4	2294	365.1
5	3790.1	603.22

Using orthogonality, the external force can be simplified to the expression

$$F_i(t) = \frac{F_0}{\rho A}\sin(\omega t) X_i(L_f) \qquad (2.32).$$

The convolution integral for any arbitrary input to evaluate q_i is in the form:

$$q_i(t) = \frac{1}{\omega_{di}} e^{-\zeta\omega_{ni}t} \int_0^t F_i(\tau) e^{\zeta\omega_{ni}\tau} \sin(\omega_{di}(t-\tau))d\tau \qquad (2.33)$$

where ω_d is the damped natural frequency and ζ is the damping ratio. The most common damping ratio values fall between 0.01 and 0.05 (Inman [2000]). For simplicity, the damping ratio will be assumed to be the average of this range, 0.03, for the beam and plate models unless otherwise specified. Equation 2.29 can now be evaluated.

The next step is to calculate the beam curvature. The curvature of the beam can be estimated as

$$\kappa(x,t) = \frac{\partial^2 w(x,t)}{\partial x^2} \tag{2.34}$$

To eliminate the dependence of length from the expression, the average curvature was evaluated as

$$\overline{\kappa}(t) = \frac{1}{L_p}\int_0^{L_p} \kappa(x,t)\,dx \tag{2.35}$$

where the limits of integration are the lengths along the beam where the PZT starts and ends. Finally, the applied moment acting on the beam is

$$M(t) = E_b I_b \overline{\kappa}(t) \tag{2.36}$$

For the time being the external force's magnitude, F_0, will be set to 1. In Chapter 4, the force magnitude will be changed to coincide with the experimental results. Substituting equation (2.36) into (2.12), (2.18), and (2.24) leads to three different expressions for the time dependent PZT voltage. Figure 2.10 shows the three signals with a phase shift of 90 degrees which coincides with the phase shift measured by the Impedance Analyzer. The voltages calculated from the Pin-force and Enhanced pin-force methods closely match each other. Though the Pin-force method assumes that the strain in the PZT remains constant and the Enhanced pin-force method considers an increasing linear strain through the PZT, the PZT is so thin that both methods produce strain values relatively close to one another. The Euler Bernoulli method produces a voltage that is more than half the other two voltages because it does not erroneously assume that the PZT bends on its on neutral axis. The Euler Bernoulli is shifted 180 degrees because of the negative sign in the moment equation.

Next, the power for each of the three methods is calculated. To generate the maximum power, the load impedance is set to equal the internal PZT impedance of

330000Ω as discussed in section 2.4. Figure 2.11 shows the relationship between power and external load impedance. The maximum power occurs at $330k\Omega$. Also, only the steady state portion of the response is used. The power values will be less if the transient response is utilized because the voltage signal has not reached its maximum magnitude. The equation used to calculate power from an AC voltage signal is

$$P = \sum_{i=0}^{n} \frac{V^2(t_i)R_L}{(R_L + R_S)^2 n} \tag{2.37}$$

where V_S is the source voltage, and n is the number of time steps.

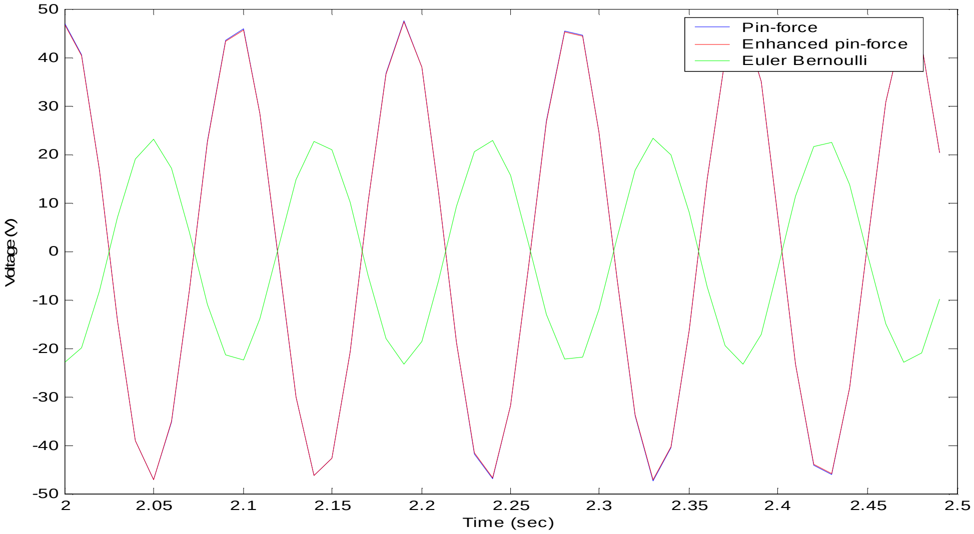

Figure 2.10. PZT voltages calculated from analytical beam model.

Table 2.3 shows the power calculated from each method. The power produced using the Euler Bernoulli method is lower than the other two values of power. This is because of the key factor of the Euler Bernoulli method correctly assuming that the PZT does not bend on its own neutral axis but bends on another shifted neutral axis. These three power values are the maximum possible powers for the factors and dimensions given.

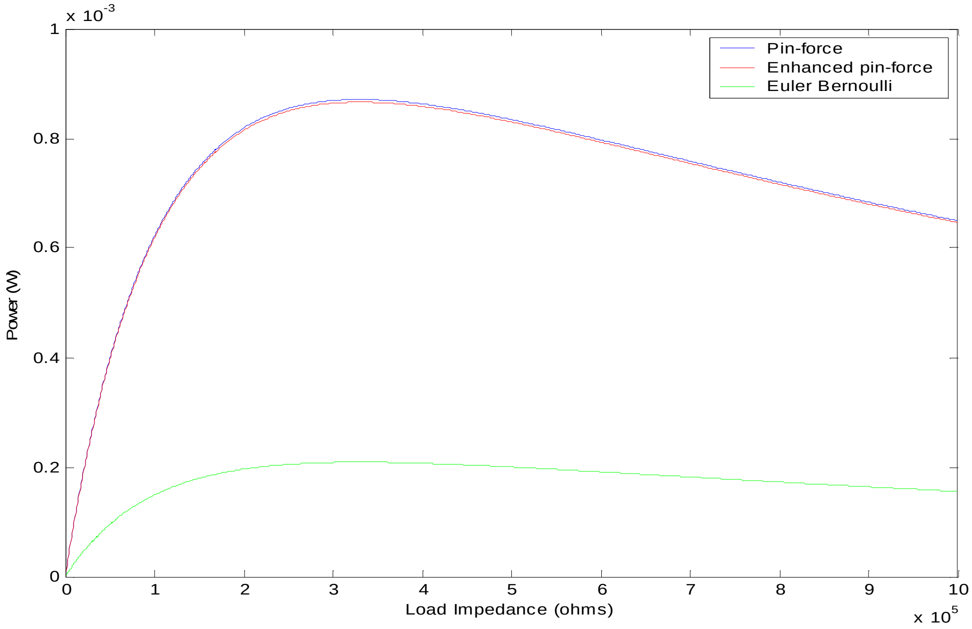

Figure 2.11. Generated power is based on external load impedance values.

Table 2.3. Power values for beam excited by harmonic force.

Method	*Power* (μW)
Pin force	870
Enhanced Pin force	866
Euler Bernoulli	209

Beam with a random noise driving force

Now, consider the external driving force to have random noise content instead of sinusoidal or any other definitive content. A function, $F(t)$, is often characterized as being random if the value of $F(t)$ for a given value of t is known only statistically (Inman [2000]). The random noise function is given by

$$F(t)=\sum_{i=0}^{n}F_0\sin\left(\omega_{rand}t-\Theta_{rand}\right) \tag{2.38}$$

where, ω_{rand} is any possible frequency within an arbitrary frequency range, Θ_{rand} is any possible phase shift with values between 0 and 2π, and n is the arbitrary number of iterations that create a sufficiently random function.

There is two different ways MATLAB can generate a random signal. The first is a summation of random sine waves. For MATLAB to produce an adequately random driving force, fifty sine functions with random frequencies and phases were chosen to be summed together. The random noise signal is simulated by using MATLAB's random number generator and the equation:

$$F(t) = \sum_{i=1}^{50} A\sin(R_{rand}\,2\pi f_{arb}t - R_{rand}\,2\pi) \tag{2.39}$$

where R_{rand} is a random number between 0 and 1 generated by MATLAB, and f_{arb} is any frequency that falls within an arbitrarily set range of frequencies. The magnitude of the signal will also vary randomly according to what frequencies and phase shifts are generated at every time step. The second method is to generate a random sine function for every time step in a data block. The method is shown by the following MATLAB code:

```
Force = [];
for t = 0:.001:3
Force_i = A*sin(rand(1)*freqrange*t-rand(1)*2*pi);
Force = [Force Force_i];
end
t = 0:.001:3;
```

This method allows the random signal to have a constant magnitude, F_0, though the frequency and phase will still vary. With either method, it can be expected that the maximum power calculated will be less than the power calculated from the harmonically driven beam because of this random assignment of driving frequencies,. As the arbitrary frequency range, f_{arb}, increases, the power produced will decrease.

The process for calculating power from random vibrations remains the same except that the forcing function is changed. The first method for generating a random noise signal is used. Since the external forcing function in random in nature, the power values change for each run of the simulation. Therefore, an average of typical values are presented in Table 2.4. The power values listed are averages of five simulations. When the $f_{arb} = 100Hz$, the power values are an order of magnitude larger than when $f_{arb} = 1000Hz$. These values are 1 – 2 orders of magnitude less than the power calculated from the harmonic external driving force. Limiting or if possible controlling the input forcing function's frequency range will increase the potential power output of a system.

Table 2.4. Average power from external random force

Method	*Power* (μW)	
	$f_{arb} = 100Hz$	$f_{arb} = 1000Hz$
Pin force	68.73	3.71
Enhanced Pin force	66.36	3.69
Euler Bernoulli	16.48	0.89

2.5.2 Analytical power estimation: cantilever plate model

The second structure modeled is a cantilever rectangular plate seen in Figure 2.12. An additional dimension is added when modeling a plate versus a beam. Because the length to width ratio is much less, the width (or y-coordinate) cannot be ignored. Another factor also cannot be ignored in the plate model as it was in the beam model. Because the PZT's cross-sectional area relative to the beam's cross-sectional area was small, the PZT would not significantly increase the stiffness of the beam structure. However, on the aluminum plate model the PZT covers one entire side of the plate. The PZT modulus is $62\times10^{9}\,Pa$ while the aluminum plate's modulus is $71\times10^{9}\,Pa$. In order to model the structure more accurately, an equivalent Young's Modulus was calculated using

$$E_{stiff} = \frac{E_b t_b + E_a t_a}{t_b + t_a} \tag{2.40}$$

where E_b and t_b are the plate's Young's Modulus and thickness, respectively. The combined modulus calculated is $68.943 \times 10^9\, Pa$. Table 2.5 gives the plate and PZT properties used in this section.

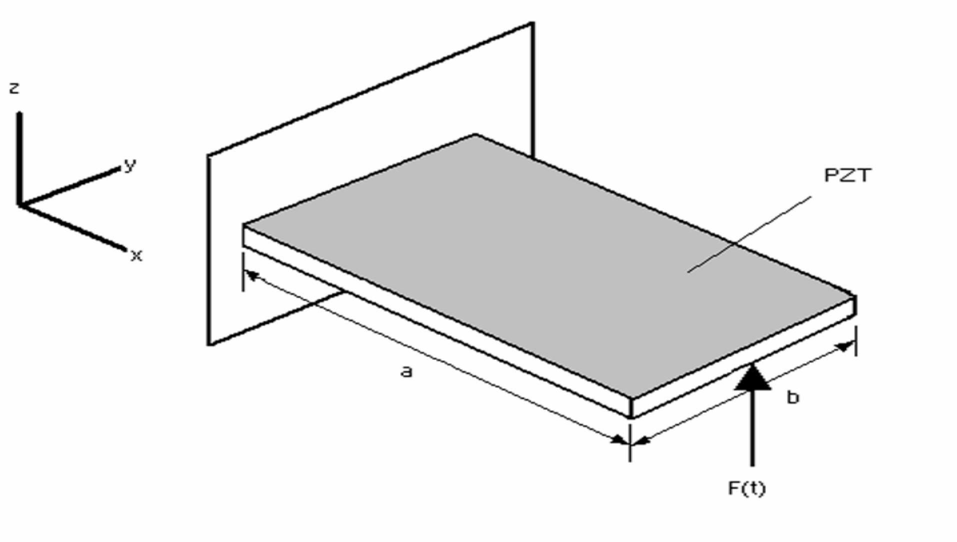

Figure 2.12. Setup of cantilever plate model. The PZT covers the entire top side of the plate.

Table 2.5. Properties and dimensions for the analytical plate model.

	Parameter	*Value*	*Units*
Plate	length	0.063	m
	width	0.040	m
	thickness	9×10^{-4}	m
	density	2715	kg/m^3
	Young's Modulus	71×10^9	Pa
PZT	length	0.063	m
	width	0.040	m
	thickness	2.667×10^{-4}	m
	Young's Modulus	62×10^9	Pa
	dielectric constant	-320×10^{-12}	m/V
	voltage constant	-9.5×10^{-3}	Vm/N
	internal resistance	3900	Ω

To solve for the natural frequencies of the plate, the Ritz method described by Blevins (1950) is used. For a vibrating uniform plate, the maximum potential energy is given by

$$V = \frac{D}{2}\iint\left[\left(\frac{\partial^2 w}{\partial x^2}\right)^2 + \left(\frac{\partial^2 w}{\partial y^2}\right)^2 + 2\upsilon\frac{\partial^2 w}{\partial x^2}\frac{\partial^2 w}{\partial y^2} + 2(1-\upsilon)\left(\frac{\partial^2 w}{\partial x \partial y}\right)^2\right]dxdy \qquad (2.41)$$

where $w(x, y)$ is the vibration amplitude, υ is the average Poisson's ratio for aluminum with a value of 0.3 (Beer [1992]),

$$D = \frac{Et^3}{12(1-\upsilon^2)} \qquad (2.42)$$

and is the plate bending stiffness, and t is the total thickness of the PZT and plate. This thickness is defined as the plate thickness. The PZT's thickness is added into the total thickness because it covers the entire area of one side of the plate and therefore will affect the properties and characteristics of the plate. When the voltages are calculated using equations (2.12), (2.18), and (2.24), a disparity will be created because of the variable Ψ, which contains a ratio of total thickness to PZT thickness, which is a portion of the total thickness.

The plate's equation for vibration is

$$D\nabla^4 w(x, y, t) - \rho w_{tt}(x, y, t) = F(t) \qquad (2.43)$$

where

$$\nabla^4 = \frac{\partial^4}{\partial x^4} + 2\frac{\partial^4}{\partial x^2 \partial y^2} + \frac{\partial^4}{\partial y^4} \qquad (2.44)$$

Much like a beam's vibrational magnitude, a plate's vibrational magnitude (Young [1950]), $w(x, y)$, can take the form

$$w(x, y) = \sum_{m=1}^{p}\sum_{n=1}^{q} A_{mn} X_m(x) Y_n(y) \qquad (2.45)$$

where A_{mn} is a coefficient that will be divided out when the determinant of the system is calculated.

The mode shapes are now calculated. Plate mode shapes can be thought of as a combination of two beam mode shapes. A beam's length that lies on the x-axis represents the plate's length, and a beam's length that is parallel to the y-axis represents the plate's width. A representation is shown in Figure 2.13.

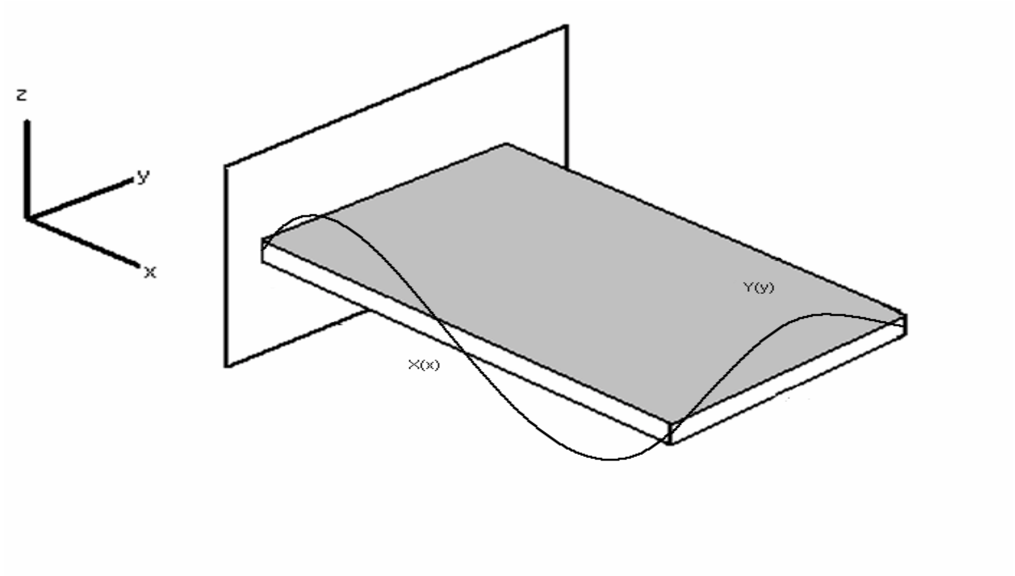

Figure 2.13. Plate mode shapes are a multiplication of two orthogonal beams with proper boundary conditions.

The plate has clamped-free boundary conditions in the x-direction:

$$\text{At } x = 0: \quad w = 0 \text{ and } w_x = 0$$

$$\text{At } x = a: \quad EIw_{xx} = 0 \text{ and } [EIw_{xx}]_x = 0$$

and free-free boundary conditions in the y-direction:

$$\text{At } y = 0 \text{ and } y = b: \quad EIw_{xx} = 0 \text{ and } [EIw_{xx}]_x = 0$$

The clamped-free modes are given by the equation

$$X_i(x) = \cosh\frac{\lambda_i x}{a} - \cos\frac{\lambda_i x}{a} - \alpha_i\left(\sinh\frac{\lambda_i x}{a} - \sin\frac{\lambda_i x}{a}\right) \tag{2.46}$$

where, the coefficients α_i and λ_i are found from Table 1 in Young (1950) and a is the length of the plate. The free-free modes are given by the equation

$$Y_i(y) = 1 \tag{2.47a}$$

$$Y_i(y) = \sqrt{3}\left(1 - \frac{2y}{b}\right) \tag{2.47b}$$

$$Y_i(y) = \cosh\frac{\mu_i y}{b} + \cos\frac{\mu_i y}{b} - \beta_i\left(\sinh\frac{\mu_i y}{b} + \sin\frac{\mu_i y}{b}\right), \qquad (i = 3,4,5,...) \tag{2.47c}$$

where the coefficients β_i and μ_i are found from Table 1 in Young (1950) and b is the width of the plate. Equation (2.47a) and (2.47b) represent the rigid-body translation and rotation, respectively, while (2.47c) satisfies the free-free boundary conditions. Table 2.6 shows the correct combination of $X_i(x)$ and $Y_i(y)$ for a rectangular plate.

Table 2.6. Mode shapes for rectangular, cantilever plate.

Mode, $\Phi(x, y)$	Pairings
1	$X_1(x)Y_1(y)$
2	$X_1(x)Y_2(y)$
3	$X_2(x)Y_1(y)$
4	$X_2(x)Y_2(y)$
5	$X_1(x)Y_3(y)$

Next, it is necessary to evaluate the following integrals:

$$E_{im} = a\int_0^a X_i \frac{d^2 X_m}{dx^2} dx \tag{2.48a}$$

$$E_{mi} = a\int_0^a X_m \frac{d^2 X_i}{dx^2} dx \tag{2.48b}$$

$$H_{im} = a\int_0^a \frac{dX_i}{dx}\frac{dX_m}{dx} dx \tag{2.48c}$$

$$F_{kn} = b\int_0^b Y_k \frac{d^2 Y_n}{dy^2} dy \tag{2.48d}$$

$$F_{nk} = b\int_0^b Y_n \frac{d^2 Y_k}{dy^2} dy \tag{2.48e}$$

$$K_{kn} = b\int_0^b \frac{dY_k}{dy}\frac{dY_n}{dy} dy \tag{2.48f}$$

where $i, k, m,$ and n are from 1 to 6. And when completed the equations (2.48a-f) make six-6×6 matrices of the same name. After some derivation, Blevins arrives at the characteristic equation:

$$\sum_{m=1}^{p} \sum_{n=1}^{q} \left[C_{mn}{}^{(ik)} - \Lambda \delta_{mn}\right] A_{mn} = 0 \tag{2.49}$$

where

$\Lambda = \dfrac{\omega^2 \rho t a^3 b}{D}$ and $\delta_{mn} = 1$ for $mn = ik$ and 0 for $mn \neq ik$. The matrix C is made from the equations (2.48a-f) by the following two equations:

$$C_{mn}{}^{(ik)} = \upsilon \frac{a}{b}\left(E_{mi} F_{kn} + E_{im} F_{nk}\right) + 2(1-\upsilon)\frac{a}{b} H_{im} K_{kn} \tag{2.50}$$

which is valid for the off-diagonal terms ($mn \neq ik$). For the diagonal terms ($mn = ik$),

$$C^{(ik)}{}_{ik} = \frac{b}{a}\lambda_i{}^4 + \frac{a^3}{b^3}\mu_k{}^4 + 2\upsilon \frac{a}{b} E_{ii} F_{kk} + 2(1-\upsilon)\frac{a}{b} H_{ii} K_{kk} \tag{2.51}$$

The determinant of this matrix must vanish and the natural frequencies, ω, will be found. Table 2.7 shows the five natural frequencies calculated by the Ritz method Young (1950).

Table 2.7. Plate natural frequencies.

Natural frequency	rad/s	*Hz*
1	1274	202.8
2	5038	802
3	6609	1052
4	16160	2571
5	23430	3729

Now that the natural frequencies and mode shapes are determined, the particular solutions to external forces can be calculated for both harmonic and random excitations.

Plate with a Harmonic Driving Force

Power from the plate driven by an external harmonic force will now be calculated. The external force is given by

$$F_i(t) = F_0 \sin(\omega_{dr} t)\delta(x - L_{x,f})\delta(y - L_{y,f}) \tag{2.52}$$

where F_0 is the magnitude of the forcing function, ω_{dr} is the driving frequency, and $L_{x,f}$ and $L_{y,f}$ are the distance of the forcing function along the beam length and width, respectively. Again, just as in equation (2.30), (2.52) can be reduced by orthogonality to the expression:

$$F_i(t) = \frac{F_0}{m} \sin(\omega_{dr} t) X_i(L_{x,f}) Y_i(L_{y,f}) \qquad (2.53).$$

where $m = \rho_a t_a + \rho_b t_b$, $L_{x,f} = a$, and $L_{y,f} = 0.5b$ for this analytical model. The convolution integral presented in equation (2.33) will be used to calculate the modal deflection, $q_i(t)$. The spatial deflection is then calculated by the expression given as

$$w(x,y,t) = \sum_{i=1}^{5} q_i(t)\Phi_i(x,y) \qquad (2.54).$$

It is interesting to note that when the plate is excited by the first natural frequency, only the odd numbered modes are excited. Therefore, the modal deflections, $q_2(t)$ and $q_4(t)$, equal zero which reduces the number of modes used in the deflection calculation to three which is consistent with the beam model. The curvatures of the plate in the x- and y-directions can now be calculated using the following equations:

$$\kappa_x(x,y,t) = \frac{\partial^2 w(x,y,t)}{\partial x^2} \qquad (2.55a)$$

$$\kappa_y(x,y,t) = \frac{\partial^2 w(x,y,t)}{\partial y^2} \qquad (2.55b).$$

As with the plate's mode shapes, the total plate curvature can be found by simply multiplying the two separate curvatures together given by

$$\kappa_{x,y}(x,y,t) = \kappa_x(x,y,t)\kappa_y(x,y,t) \qquad (2.56).$$

To eliminate the curvature's dependence of position on the plate, the average curvature was calculated as

$$\bar{\kappa}(t) = \frac{1}{ab}\int_0^b \int_0^a \kappa_{x,y}(x,y,t)\,dx\,dy \qquad (2.57).$$

This complex expression could not be solved analytically. To achieve an expression for $\bar{\kappa}(t)$, a simplification is made. Of the three mode shapes under consideration only mode 5 has a dependence on width, or the variable y. Modes 2 and 4 depend on the variable y but do not contribute to the curvature because they are not excited; therefore, only considering modes 1 and 3 gives a suitable result for the average curvature. By excluding mode 5, all dependence on the width is eliminated thus reducing equation (2.57) to

$$\bar{\kappa}(t) = \frac{1}{a}\int_0^a \kappa_x(x,t)dx \qquad (2.58).$$

Now, the moment applied to the plate can be calculated as (Timoshenko [1959])

$$M_b(t) = -D\bar{\kappa}(t) \qquad (2.59).$$

where $M_b(t)$ is the applied moment per unit width. The applied moment is multiplied by the width to get units of *Nm* and is shown by

$$M(t) = -Db\bar{\kappa}(t) \qquad (2.60)$$

Substituting equation (2.60) into (2.12), (2.18), and (2.24) gives the voltage expressions for the three different methods. To obtain the maximum power, an Impedance Analyzer is used to find the internal impedance of the PZT at the plate's first natural frequency. The PZT's internal impedance is 3900Ω. The power is calculated for each method using equation (2.37). Figure 2.14 shows the calculated power and its relationship with the load impedance. As expected, the maximum power occurs when the load impedance has the same value as the internal resistance of the PZT. The power calculated from each method is shown in Table 2.8. The Euler Bernoulli method gives a power value two orders of magnitude lower than the other two powers.

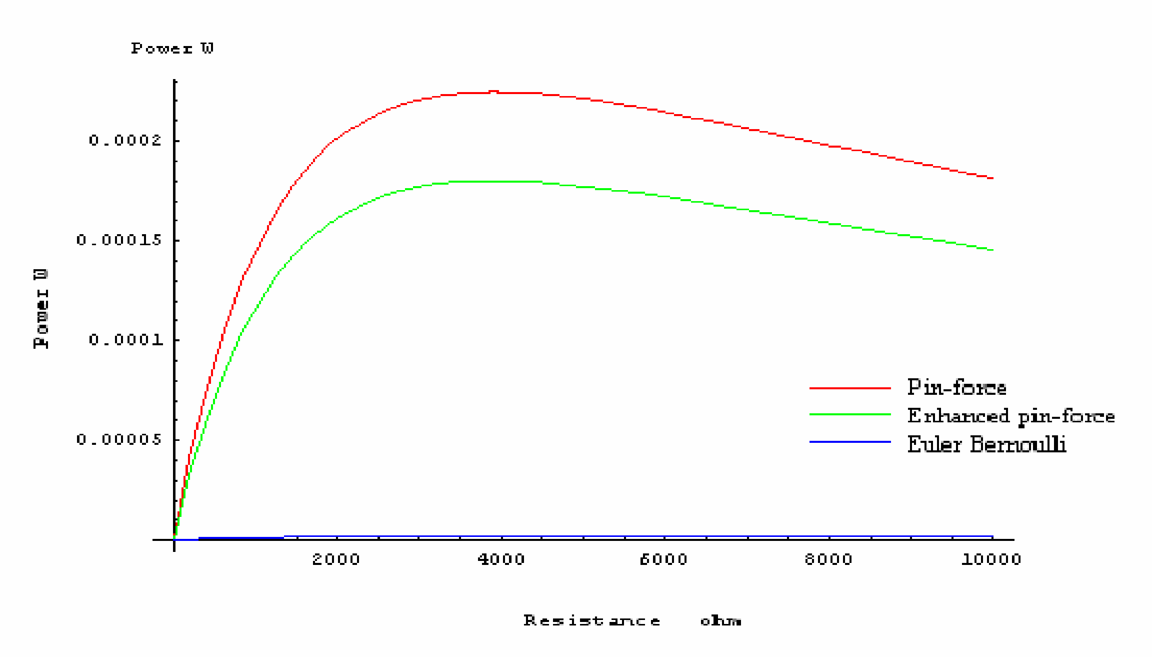

Figure 2.14. Power varies according to the value of the load impedance.

Table 2.8. Average power from a plate driven by an external harmonic force.

Method	*Power* (μW)
Pin force	224.6
Enhanced Pin force	180.1
Euler Bernoulli	2.178

Plate with a Random Noise Driving Force

The harmonic forcing function is now replaced by a random noise signal, given by equation (2.38). The frequency range used is 0-1000Hz so that the first and second resonant frequencies are included within the range of possible frequencies. Because of the added dimension of width in the plate calculation and of the high number of iterations used to assure a random force, Mathematica can not readily solve the convolution integral as shown in the previous section.

In order for Mathematica to solve for the power generated from random excitations, an alternate process had to be followed. To simplify the convolution integral, the external forcing functions that make up the random signal content are not summed as in equation (2.38). Instead, the modal deflection is summed in the expression given by

$$q_i(t) = \frac{X_i(a)Y_i(\frac{b}{2})}{m\omega_{di}} e^{-\zeta\omega_{ni}t} \sum_{\omega=1}^{50} \int_0^t F(\tau) e^{\zeta\omega_{ni}t} \sin(\omega_{di}(t-\tau)) d\tau \qquad (2.61).$$

This equation simplifies the integral by removing the summation from inside the convolution integral to the outside. With the summation inside the integral, the forcing function is fixed with n, or in this case 50, random sinusoidal functions which remain the same for $i = 1:5$. With the summation outside the integral, the drawback is that the forcing function will now be different every time the integral is evaluated. So, the plate's first mode will be excited by a totally different random force than the other plate modes. Fortunately, since the magnitude and the possible frequency range do not change, and because the first mode is the most dominant mode when a structure is excited, the simplification should produce comparable values of modal deflection.

An alternate equation for curvature is also developed and given by

$$U_i(x,y) = \frac{d^2 X_i(x)}{dx^2} \qquad (2.62)$$

$$\overline{\kappa}(t) = \sum_{i=0}^{4} q_i(t) \frac{1}{ab} \int_0^b \int_0^a U_i(x,y) dx dy \qquad (2.63).$$

The moment applied to the plate by the random force is given by equation (2.60). The equations for voltage are (2.12), (2.18), and (2.24). Again, equation (2.37) is used to calculate power for the three different methods. The resulting power values are shown in Table 2.9.

Table 2.9. Average power from a plate excited by random noise.

Method	*Power (μW)*
Pin force	178.2
Enhanced Pin force	142.9
Euler Bernoulli	1.728

2.6 Conclusions

To produce maximum power from piezoelectric elements which are attached to vibrating structures, the structures should be excited at their first natural frequency where they experience the largest deflections. Random excitations reduce the potential power that can be produced from the structures vibrations. As the bandwidth of possible frequencies excited decreases, the potential power output increases.

The next chapter will discuss the optimal length and position of the PZT on a beam structure, optimal substrate thickness, and the optimal location for the forcing function as well. Note that if part or all of the PZT is located father along the beam than the position of where the forcing function is applied, then that part of the PZT will not experience strain related to the applied force. This may reduce the potential power output of the PZT.

Chapter 3

Parametric study of beam and PZT structure

3.1 Introduction

This chapter deals with a parametric study of several variables in order to determine how the power is affected by the variables and to optimize the potential power output of the PZT attached to a beam. The beam and PZT system used in Chapter 2 will be the basis of the parametric study except for two changes. To simplify the parametric calculations, the beam length will be rounded to $0.550m$ and the PZT length will be shortened to $0.05m$. The study will examine different PZT locations along the beam. The PZT length and thickness, along with the beam thickness, will be studied and optimized. The position of the external forcing function will be optimized for maximum output as well. Finally, the power produced using these optimized values will be calculated.

3.2 Optimization of variables

This section develops a relationship between several variables and output power as well as optimizes the variables to produce the maximum power output of the PZT.

3.2.1 PZT location

The piezoelectric material location is important to the output power. Because the power produced by the PZT is directly related to the strain of the beam, it makes sense that the PZT should experience the largest beam strains in order to produce maximum power. The largest strain occurs at the clamped edge of the cantilever beam (Crawley

[1986]). In certain applications, attaching the PZT on or close to the clamped end of a beam is not possible. For this reason, a correlation between power and PZT location will be developed. Figure 3.1 shows how the PZT will be sequentially moved along the beam from position 1 to 11, and MATLAB will simulate the power output from each location. In this study, the PZT length is $0.05m$ and the beam length is $0.550m$. Figure 3.2 shows the power output as a function of PZT position. As expected, the highest power values are at position 1, where the PZT is closest to the clamped end and experiences the largest strains.

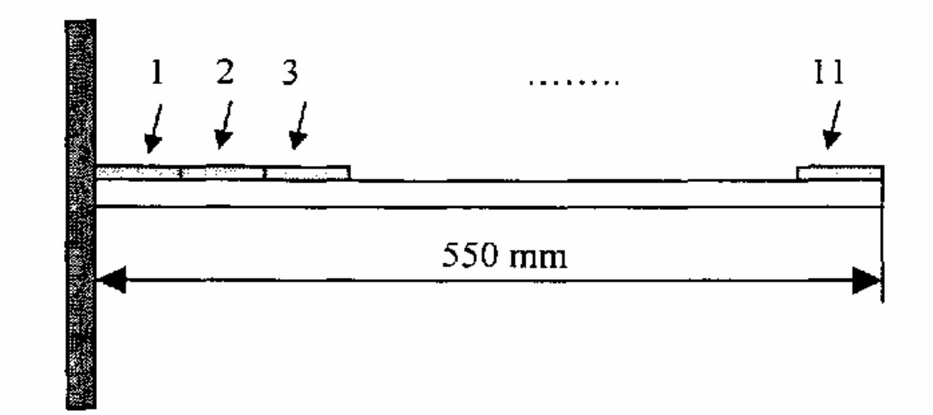

Figure 3.1. Setup of PZT and beam for a study to optimize location.

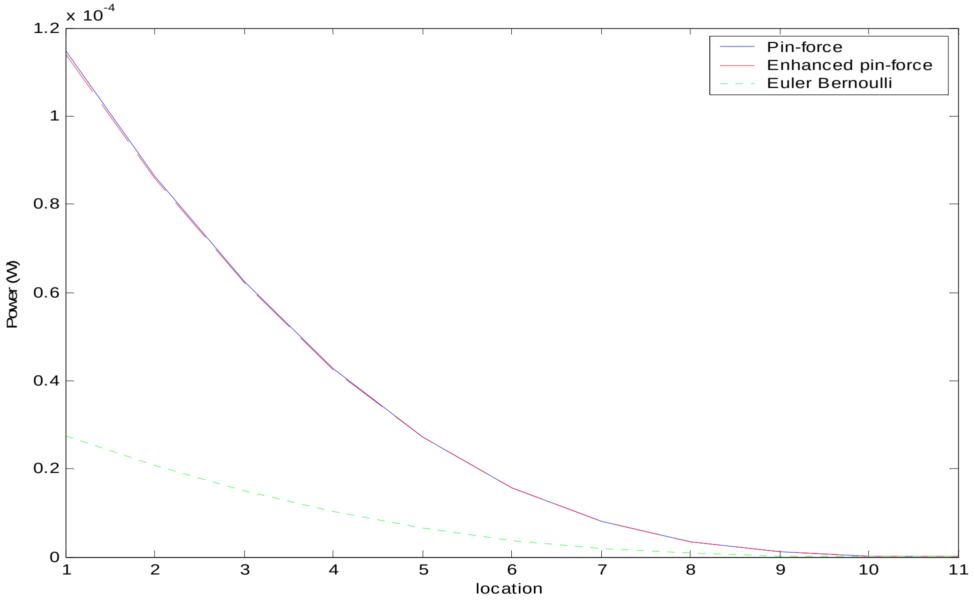

Figure 3.2. Power output of the three methods versus the 11 positions the PZT was moved along the beam.

3.2.2 PZT length

The next variable that is optimized is the PZT length. A study is performed to calculate the optimal length to produce maximum power. The setup is shown in Figure 3.3. In section 3.2.1, the optimal PZT location was found to be adjacent to the clamped end of the beam. Having one end at the beam's clamped end, the PZT will have a length, L_p, of $0.05m$ and will be increased $0.05m$ until it covers the entire length of the beam. Figure 3.4 shows the PZT length versus output power. When solving for power by using the equation given by

$$P = \frac{V^2}{R} \tag{3.1}$$

there appears to be no optimal PZT length as shown in Figure 3.4. As the PZT length decreases, the output power increases. This, however, is inaccurate. A piezoelectric material acts as a capacitor storing a charge. A capacitor's ability to store a charge is directly related to the surface area on which the charge can accumulate. So, another method must be used to incorporate surface area to determine the true optimal PZT length.

This alternate method will use the equation given by

$$P = V_{rms} I_{rms} \tag{3.2}$$

to calculate power. The current is calculated by

$$I = C_P \frac{dV}{dt} \tag{3.3}$$

where C_P is the PZT effective capacitance given by

$$C_P = \frac{d_{31} A_{surf}}{g_{31} t_a} \tag{3.4}$$

where d_{31} is the piezoelectric strain coefficient of the piezoelectric element and A_{surf} is the surface area of the piezoelectric element. Figure 3.5 shows the output power versus PZT length calculated by using current. Larger is not necessarily better in the case of

PZT length. An optimal length of $L_p = 0.300m$, approximately when the PZT covers half the beam, produces the maximum power. By increasing the PZT surface area six times from $0.05m$ to $0.300m$, a 275% increase in power is made. A tradeoff has to be made between an increase in potential power produced and increase of PZT cost. When the PZT used reaches a certain length, it will start to affect the overall characteristics of the beam system, changing the effective cross-section, Young's modulus, and natural frequencies. This will have adverse effects, reducing the beam deflections, strain experienced by the PZT, and overall power produced.

There is a caveat in using the current to calculate power. When current is used to determine output power as in equation (3.2), the power values produced are higher than the power values produced when using equation (3.1). Equation (3.2) does not take into consideration impedance matching and the value used for C_P is an estimate.

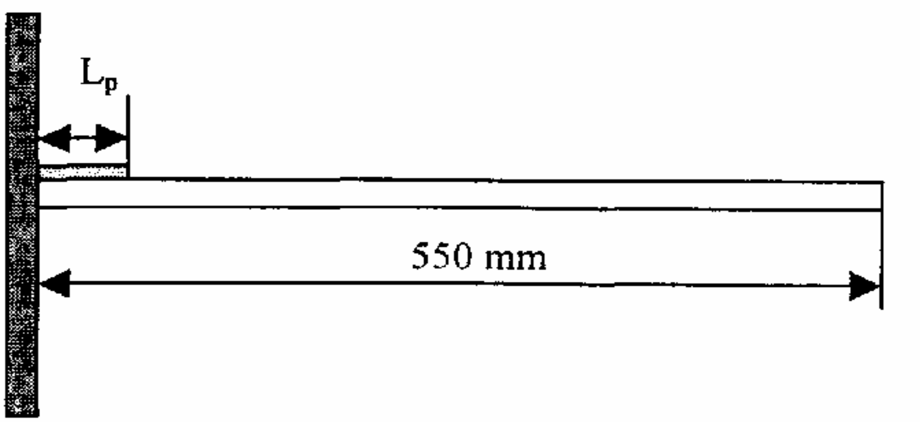

Figure 3.3. Setup of PZT and beam for a study to optimize length.

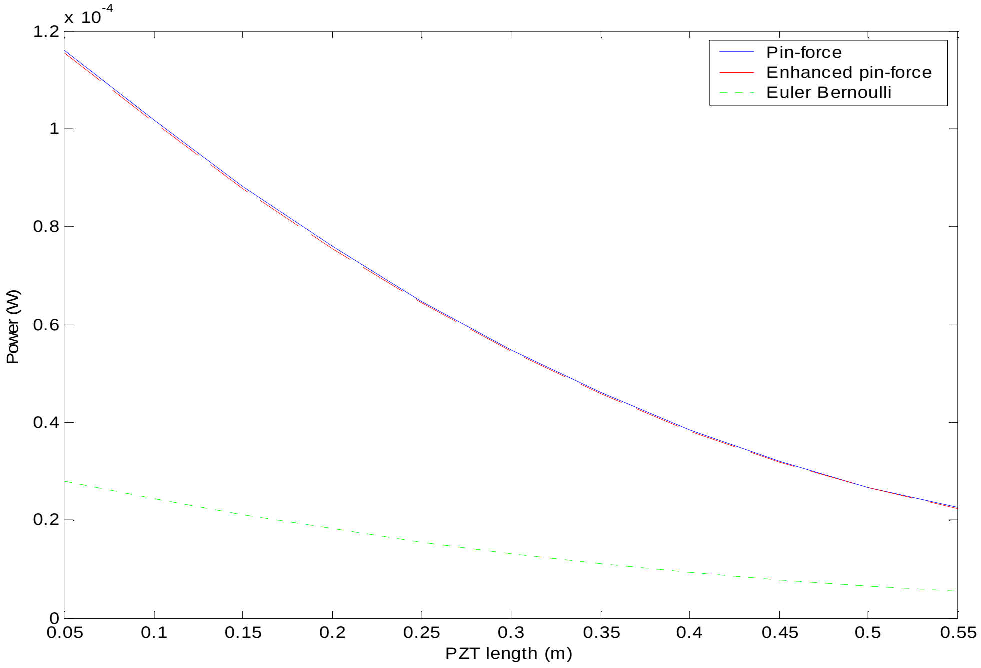

Figure 3.4. Power output versus PZT length.

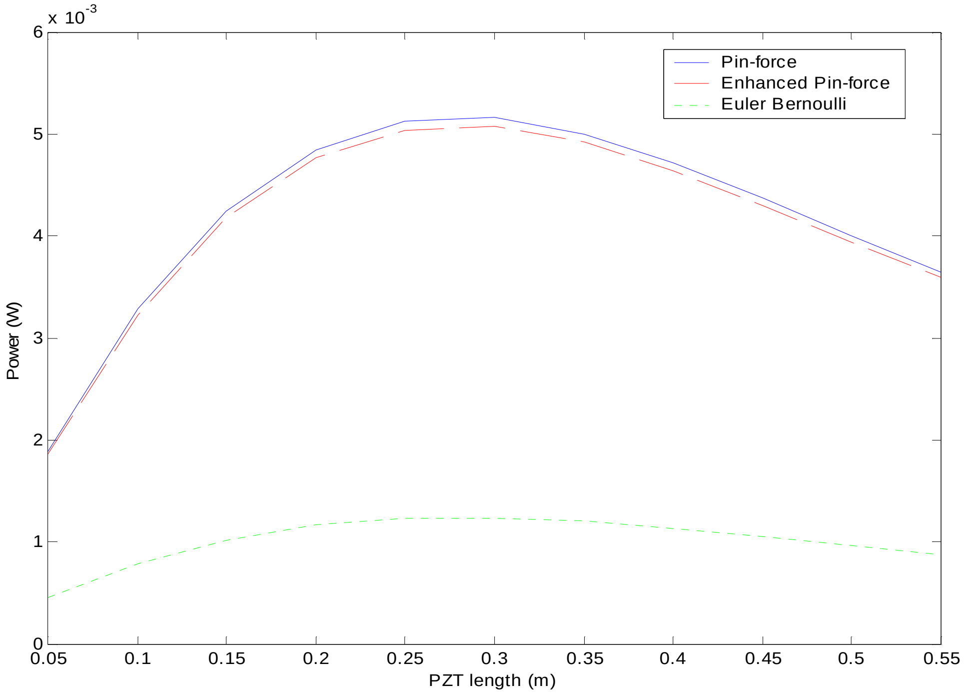

Figure 3.5. Actual output power versus PZT length.

3.2.3 *Thickness ratio*

It is beneficial to examine the ratio of the PZT thickness to the beam thickness. The three PZT modeling methods all are dependent upon this thickness ratio In Figure 3.6, the Pin-force method produces one pole at $t_a / t_b = 0.387$ while the Enhanced pin-force produces two poles at $t_a / t_b = 0.4$ and 1.5. These poles are produced by the denominator in each method equaling zero. In real world applications, all objects have damping; therefore, the power produced will not be infinite. Figure 3.7 shows the Euler Bernoulli method which is presented separately because it produces lower power values than the Pin-force and Enhanced pin-force methods. The Euler Bernoulli method which produces an optimal thickness ratio of 0.525.

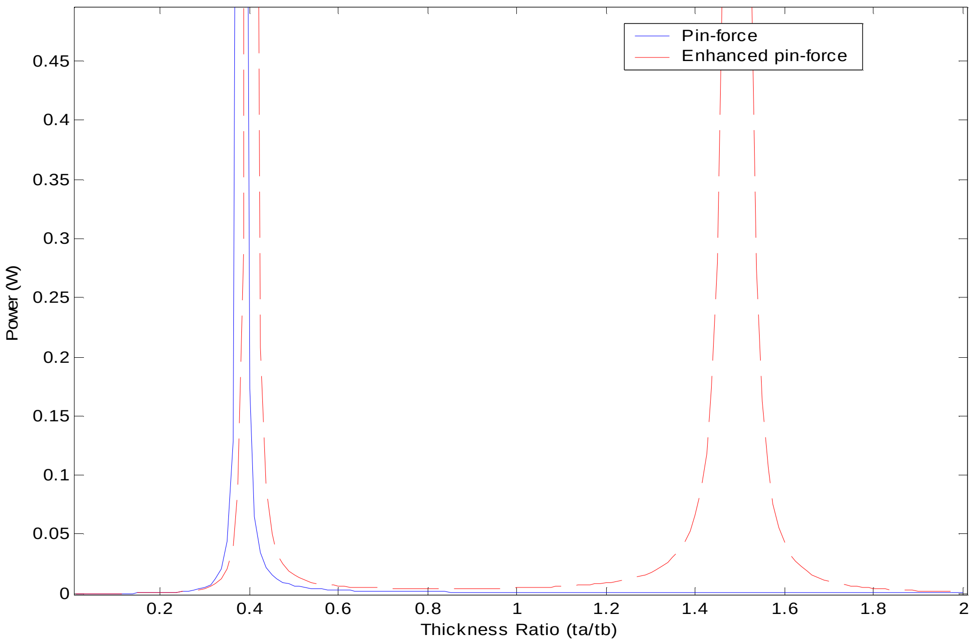

Figure 3.6. The output power of the Pin-force and Enhanced pin-force methods increases exponentially whenever the denominator of the model's equation equals zero.

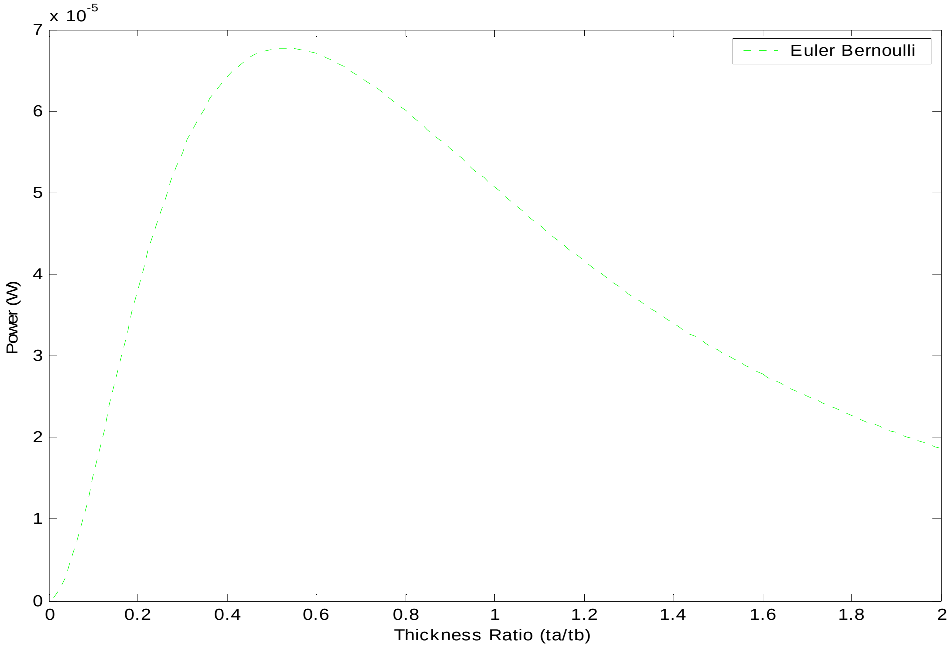

Figure 3.7. The Euler Bernoulli method has an optimal thickness ratio of 0.525.

3.2.4 Forcing function location

In Chapter 2, the forcing function in the beam analytical model was $0.200m$ from the clamped end of the beam. The output power should change according to where the forcing function is applied to the beam. For this reason, the forcing function location will be varied as shown in Figure 3.8 to determine optimal placement to maximize power. The farther away the forcing function is from the beam's clamped end, the larger the moment applied to the beam through force. So, it follows that the optimal location for the force is at the free end of the beam, which creates the largest moment. Figure 3.9 shows the power produced from the three methods.

For experimental setups, a shaker is used to simulate the forcing function. If the forcing function is located near the free end and depending on the length of the beam, the deflections of the free end may be too large to be accommodated by the shaker and its stinger. That is, the shaker may not be able to move the stinger the full range of deflection thus creating a hindering force, reducing the deflections, and distorting the voltage signal. In order to avoid this situation, the forcing function in the analytical model for the beam in Chapter 2 is located $0.200m$ from the clamped end. The beam deflection at this location is below the maximum distance the shaker can move its stinger which eliminates any external damping force created by the shaker.

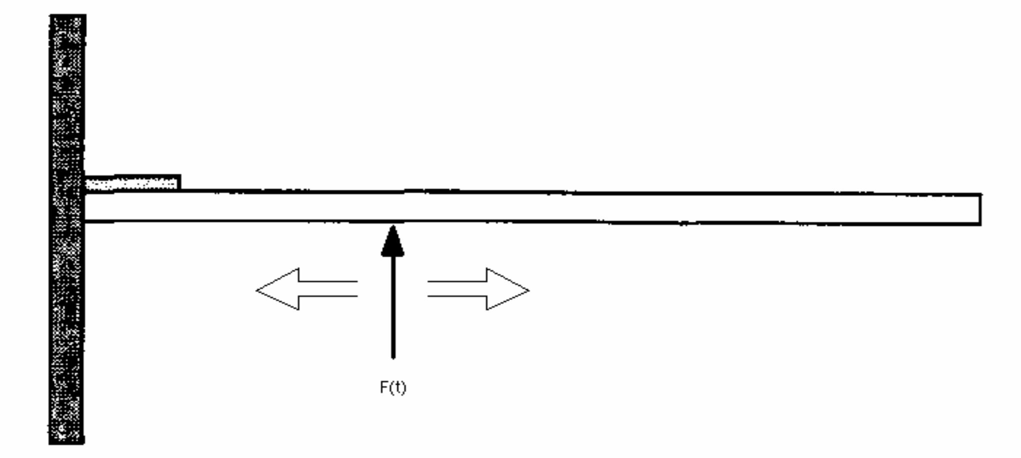

Figure 3.8. The forcing function is positioned in $0.004m$ increments over the beam length to determine the optimal location.

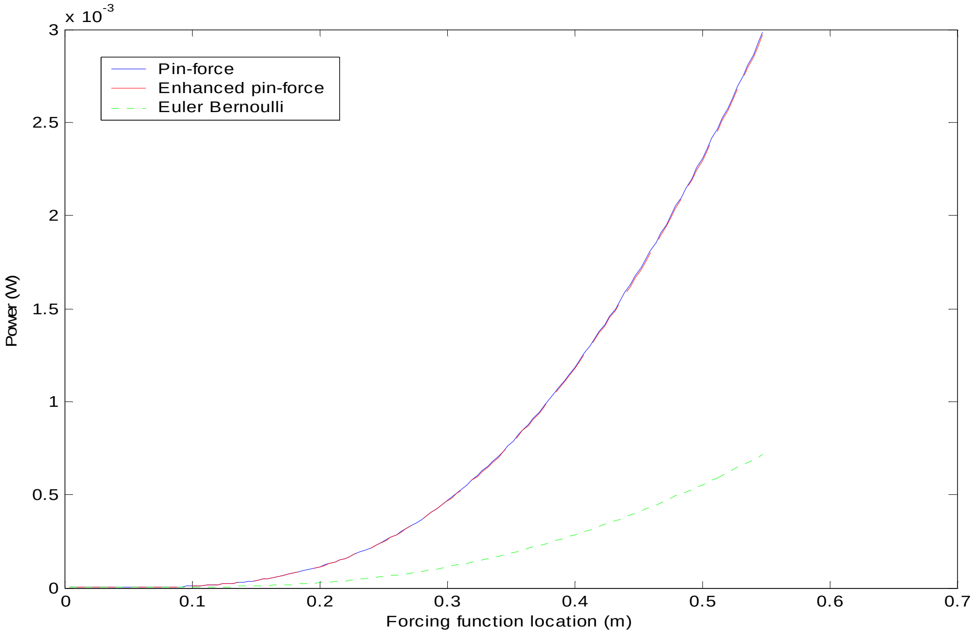

Figure 3.9. The power increases as the forcing function is located farther away from the clamped end of the beam.

3.2.5 Optimized factors used in analytical model of beam

Now, the four optimized factors will be used in the analytical model of the beam, and the maximum power from the beam will be calculated for both the harmonic and random input excitation. Though the beam used in this chapter was rounded off from $0.558m$ to $0.550m$, this section will revert back to the original beam length. The PZT location will remain the same. The PZT will be attached to the beam at the clamped end. The PZT length will be optimized to $0.300m$. The Euler Bernoulli method's thickness ratio of 0.525 will be used. The beam will be driven by the forcing function at its free end. The assumption that the shaker will not adversely affect the beam vibrations will be used for this study.

Following the process developed in Chapter 2, the power is calculated with the external force being harmonic. Figure 3.10 shows the steady-state voltage. The Pin-force and Enhanced pin-force methods have their poles very close to the optimal ratio of the Euler Bernoulli method. The voltages have increased dramatically. For this reason, the Pin-force and Enhanced pin-force methods have extremely large voltages. The Euler Bernoulli method now produces a voltage which is over 200% greater than without the optimized variables.

Table 3.1 compares the power values to the output power calculated in Chapter 2. The power values have been increased 271000%, 619000%, and 15800%, respectively. Such large power increases are misleading because the Pin-force and Enhanced pin-force methods increase to infinity with the thickness ratio while the Euler Bernoulli method has an optimal point. For this reason, only the Euler Bernoulli method should be considered reasonably accurate.

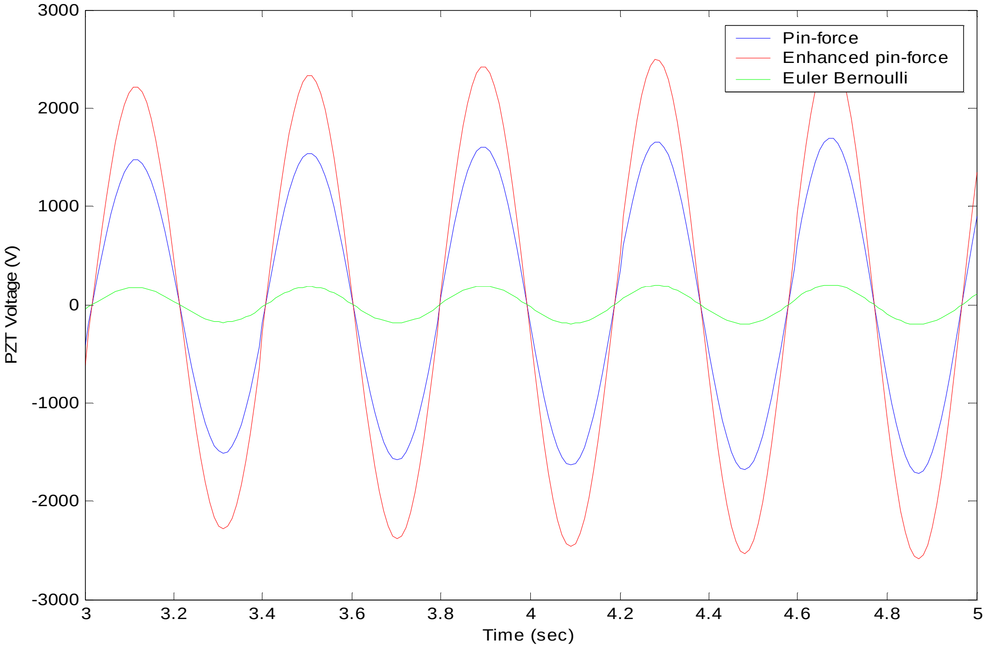

Figure 3.10. The magnitude of the steady-state voltage is increased when the optimized variables are utilized.

Table 3.1. Power values calculated from optimized variables compared to values calculated in Chapter 2.

Method	Power (mW)	
	original	*optimized*
Pin-force	0.870	2360
Enhanced pin-force	0.866	5365
Euler Bernoulli	0.209	33

Now, the external force is changed from a single harmonic function to a random harmonic function. The random vibration model developed in section 2.4.1 with the optimized variables to calculate values for power. Table 3.2 compares the power before and after the optimized variables are implemented. The frequency range, f_{arb}, is $0-100Hz$. Since the beam vibrates with the greatest magnitude when driven at the first natural frequency, the random excitation cannot cause the beam to vibrate at comparable magnitudes; therefore, the power will not increase as dramatically as with the harmonic excitation force. The power values are still increased 20500%, 48000%, and 1200%, respectively.

Table 3.2. Analytical power values before and after the optimized variables are implemented

Method	Power (μW)	
	original	*optimized*
Pin-force	68.73	14100
Enhanced pin-force	66.36	32000
Euler Bernoulli	16.48	197

3.3 Conclusions

By optimizing certain variables in the beam analytical model, power produced by the PZT should be increased. The PZT location was found to be best when the PZT was attached next to clamped end of the beam. The PZT length was optimized at a length of $0.300m$. For the Euler Bernoulli method, the PZT had an optimal thickness ratio of 0.525. The forcing function's optimal position was the farthest point from a fixed end. This would cause the largest moment to be applied to the beam, and power is directly related to the applied moment. By utilizing the optimized variables, the power produced using the Euler Bernoulli method is increased over 15000% for the harmonicly driven case and 1200% for the random noise driven case.

Chapter 4

Comparing the analytical models to experimental data

4.1 Introduction

This chapter compares the analytical models to experimental results. Experiments are performed for each of the four different analytical models. These experiments will have the same variables and values used in Chapter 2. The forcing function, voltage, and power values will be compared. Suggestions on improving the correlation between the analytical models and experimental data will be discussed. At the end of the chapter, conclusions and recommendations based on the results will be stated.

4.2 Cantilever beam experiment and comparison

This section will discuss the cantilever beam experiments and compare their results to the analytical models developed in MATLAB. First, the experimental procedure will be presented. The experiment will then be run with the harmonic forcing function. Comparison of the forcing function, deflection, voltage, and power values will be performed. This process will then be repeated for a random noise external forcing function.

4.2.1 Experimental procedure

The experiment is developed in order to test the validity and accuracy of the analytical power model of the cantilever beam. Figure 4.1 shows a picture of the experimental setup. The total length of the aluminum beam used in the experiment is $0.624m$. When one end of the aluminum beam is secured by a “C”-clamp, thus giving a clamped boundary condition, the beam length is reduced to $0.558m$. The engineering program, MATLAB, along with the Siglab toolbox is used as a function generator and data acquisition system. The external forcing function is generated as an electronic signal and sent to a Ling Dynamics Systems V203 permanent magnet shaker which translates the electronic signal into a physical signal and drives the beam. But because the function generator can only produce a voltage and very little current, the signal must first be sent through an amplifier with a gain of 1 to add current in order to power the shaker. The shaker’s stinger, the slender rod, is connected to the beam $0.200m$ along its left side by double sided 3M tape.

Figure 4.1. Experimental setup of the beam.

A PCB Piezotronics force transducer is attached to the stinger to measure the physical force that the shaker produces. The sensitivitiy of the transducer is $0.1124V/N$. The output of the piezoelectric sensor in the force transducer cannot be read correctly without first being passed through a signal conditioner. Measuring devices such as oscilloscopes and data acquisition systems have high impedances generally in the megaohms. The main purpose of signal conditioning systems acts to bridge the impedance of the piezoelectric sensor with the higher impedance of the signal processing hardware.

A piezoelectric material, model number PSI-5H43 manufactured by Piezo Systems, Inc., has dimensions $0.073x0.050m$ and is affixed to the beam's right side at the clamped end. This PZT acts as a generator, converting the mechanical strains produced from the beam's vibrations to an electrical charge.

In order to calculate power, the voltage is passed through a resistor which has the same value as the internal resistance of the PZT. For the beam excited by a harmonic forcing function this resistance is 330000Ω. The voltage drop across the resistor is measured by Siglab.

Finally, a vibrometer is used to measure the deflection. The laser vibrometer is positioned so that the laser is perpendicular to the beam and in focus. A piece of metallic copper tape is placed on the beam $0.0575m$ from the clamped end to provide a highly reflective surface for the laser. The vibrometer measures the deflection and converts the signal to voltage. The conversion factor for this application is $80\mu m/V$.

4.2.2 Experimental beam results and comparison to analytical model

This section will discuss the experimental results and comparison to the analytical model. The forcing function will first be harmonic then changed to contain random noise content. After the data was collected, MATLAB is used to process the resulting signals.

<u>Beam with a harmonic driving force</u>

A comparison of the analytical model will be made to the experimental results. The input voltage signal produced by Siglab and sent to the shaker is given by

$$F(t) = 0.5\sin\left(2\pi\left(10.6125\right)t\right) \qquad (4.1).$$

The shaker converts this electrical signal to a physical force through a coil inductor. The force transducer senses the signal shown in Figure 4.2. Earlier in Chapter 2, the forcing function magnitude, F_0, for the forcing function was given a value of 1. In the experiment, the forcing function had a magnitude of 0.5, so the F_0 in the analytical model must be adjusted. Two values, 0.3 and 0.35, for F_0 in equation given by

$$F(t) = F_0 \sin\left(2\pi(10.6125)t\right) \tag{4.2}$$

will be compared in Figure 4.2, and the value which produces the closest results for forcing function will be chosen. The dashed black signal is the force that the force transducer measures. The magnitude of 0.35 matches the ideal forcing function more closely and is therefore used in the analytical model.

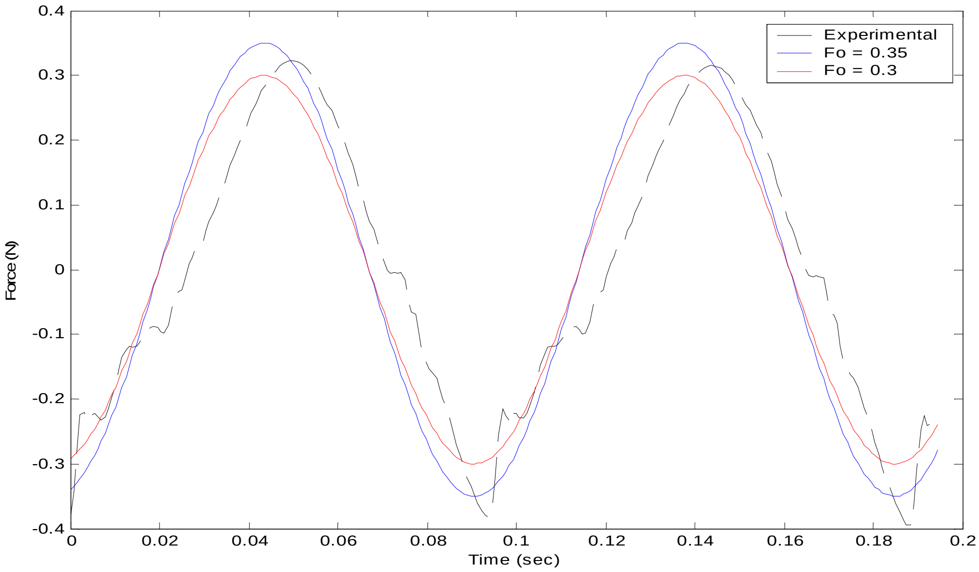

Figure 4.2. The experimental force compared to two different analytical forces.

Another good indicator of how well an analytical model predicts an experiment is the comparison of deflections experienced by the beam. Figure 4.3 shows the measured deflection of the cantilever beam $0.0575m$ from the clamped end and the analytical deflection at the same point. The experimental deflections reach $25\mu m$ while the analytical model predicts deflections of $32\mu m$. Normally, a 28% error is considered large, but because the deflections have such low values a $7\mu m$ difference is acceptable.

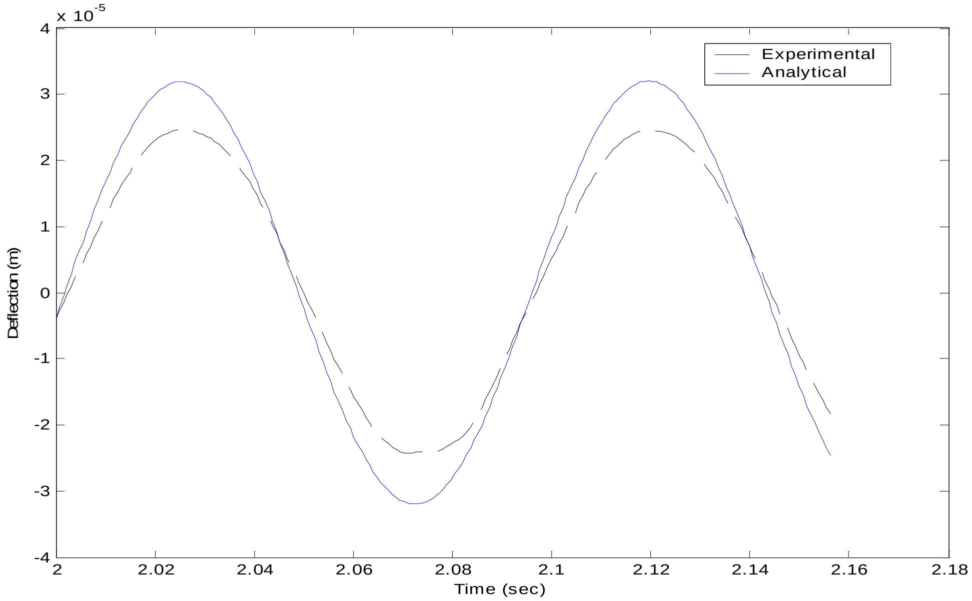

Figure 4.3. The experiment deflection at 57.5*mm* from the clamped end compared to analytical deflection at the same point.

Next to be compared are the steady-state responses of the voltages. Figure 4.4 shows the experimental and the three analytical voltage signals. The Euler Bernoulli method, with a magnitude of 8.24*V*, very accurately predicts the experimental voltage, which has a magnitude of 8.16*V*. The Euler Bernoulli method has only a 1% error. The Pin-force and Enhanced pin-force magnitudes are more than double the measured voltage's magnitude. These are not good predictors of power harvesting voltage signals.

The power values are shown in Table 4.1. The Pin-force and Enhanced pin-force methods overestimate the power capable of being produced. The Euler Bernoulli method produces a power value very close to the actual power generated by the harmonic force. It can be concluded that the Euler Bernoulli method can be used to effectively model a beam excited by a harmonic force and the power generated from the excitation of the PZT.

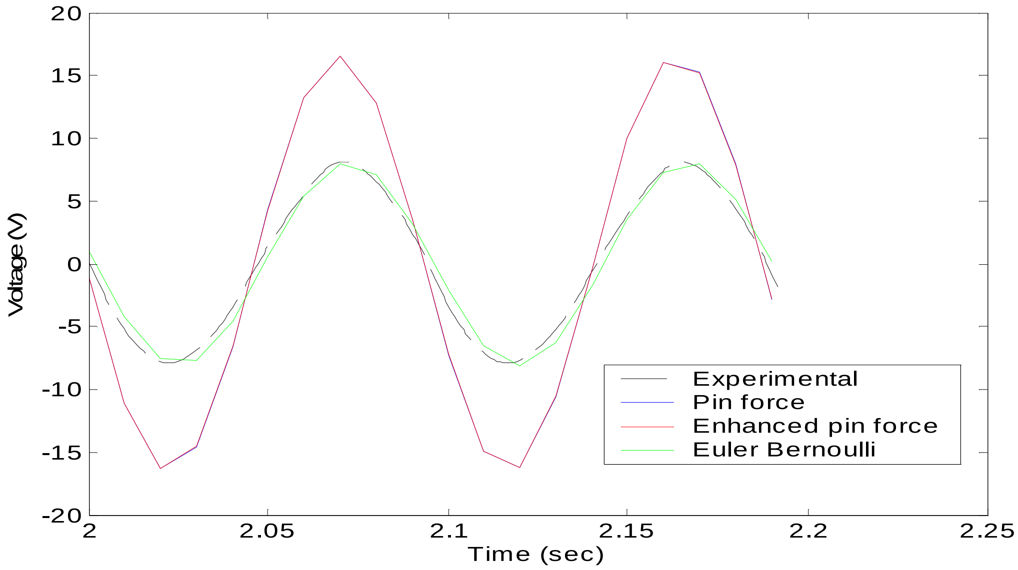

Figure 4.4. The experimental voltage compared to three different analytical voltages.

Table 4.1. The experimental power compared to three analytical powers.

Method	Power (μW)
Experimental	23.7
Pin-force	107
Enhanced Pin-force	106
Euler Bernoulli	25.6

Beam with a random noise driving force

Now the analytical model will be compared to experimental results while using a random noise driving force. Siglab was used to generate a random signal with a frequency range of $0-100Hz$. In Chapter it is shown that less power is generated from random vibrations than with a harmonic force at the first resonant frequency. For this reason the V_{RMS} value is raised from $0.354V$ for the harmonic driving force case to $0.5V$ for the random noise case. Values of output power for the random noise case should be similar to the output power calculated from the harmonic forcing function case.

Figure 4.5 shows the experimental random force which the force transducer measures and the analytical signal generated by equation (2.39). Note that the signal reaches magnitudes higher than $0.35N$, even though it has been established earlier in the section that a 0.5*V* input to the shaker will produce an approximate force magnitude of 0.35*N*. This occurs because both signals are summations of individual sine waves whose maximum magnitude is 0.35*N*. In Chapter 2, two methods are discussed for generating a random signal. The first method given by equation (2.39) is used because the measured signal has random magnitudes.

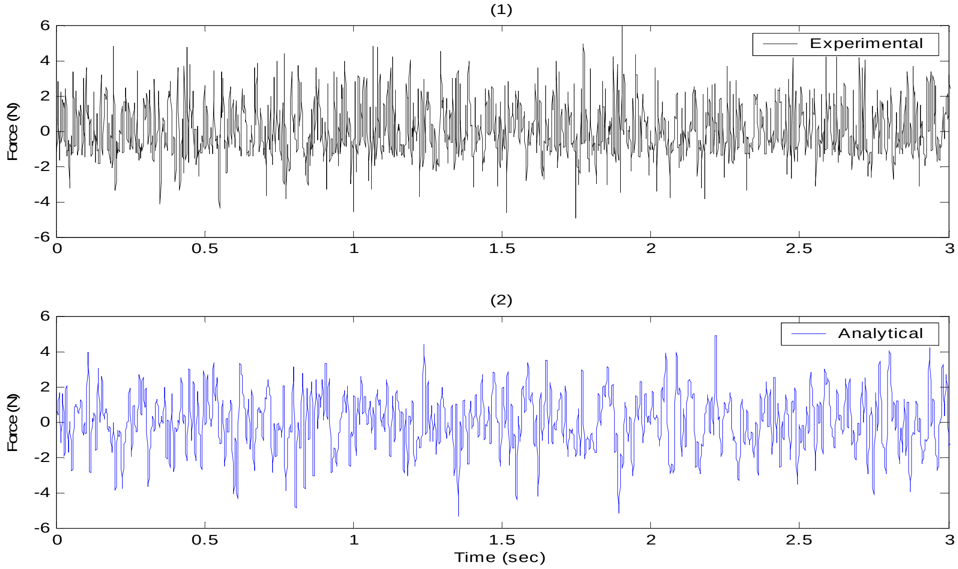

Figure 4.5. (1) Experimental force measured by force transducer. (2) Analytical model force generated by MATLAB.

Figure 4.6 shows the experimental and analytical deflections for a beam excited by a random noise force. The deflections are measured along the midline $57.5mm$ from the clamped end of the beam. The analytical deflections change directly with the forcing function; therefore, the beam deflections are not repeatable because of the random nature of the external force. The analytical deflections are on the same order of magnitude as the experimental deflections. Therefore, it is concluded that the analytical model can accurately represent beam deflections.

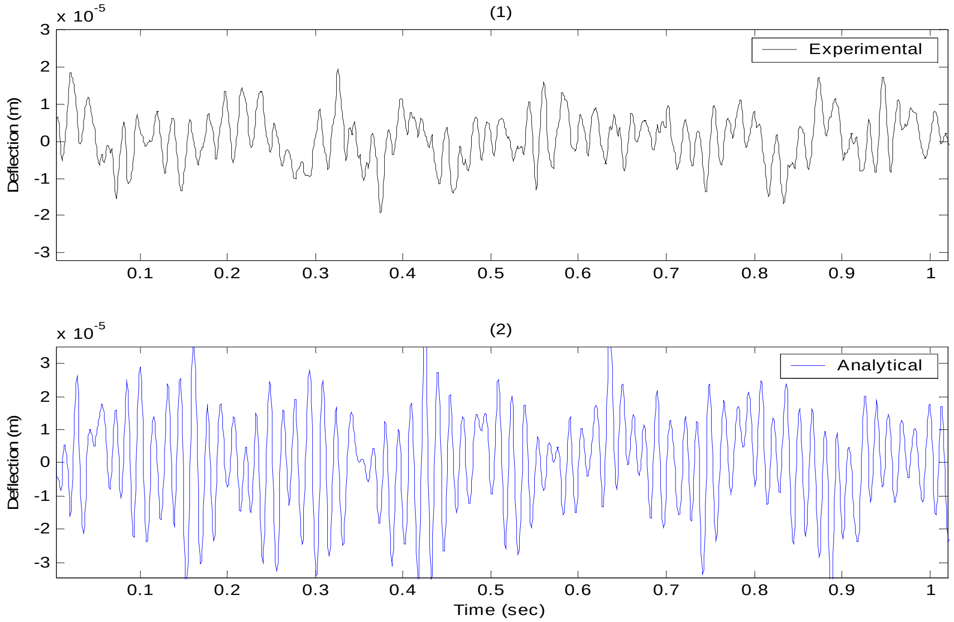

Figure 4.6. (1) Experimental deflection measured by the vibrometer. (2) Analytical model deflection generated by Euler Bernoulli method.

The voltage is compared next. The root-mean-square (RMS) voltage for the experiment and the range of RMS voltages for each of the three methods are calculated and shown in Table 4.2. The experimental voltage does not fall within the voltage range of the Pin-force and Enhanced pin-force methods. However, the experimental voltage falls within the Euler Bernoulli method's range of possible V_{RMS} values. The Euler Bernoulli method and experimental ranges overlap which validates the Euler Bernoulli method as a good predictor of the experimental results.

Table 4.2. Approximate root-mean-square voltage values for beam excited by a random noise force.

Method	V_{RMS} (V)
Experimental	3.133
Pin-force	6.55 – 15.3
Enhanced Pin-force	6.54 – 15.3
Euler Bernoulli	3.10 – 7.37

The power is the last to be compared. A range of analytical power values for each method is compared to the experimental power in Table 4.3. The experimental power value of $7.44\mu W$ is not included in the ranges for the Pin-force and Enhanced pin-force methods. However, it does fall in the Euler Bernoulli power value range. Figure 4.7 shows the voltage and corresponding power values for the Euler Bernoulli method. By interpolation, the analytical model can be seen to produce a power value of $7.3\mu W$ from a voltage of $3.1V$. For this reason, it can be concluded that the Euler Bernoulli method is a reasonable predictor of experimental results for power generation.

Table 4.3. Experimental power compared to an average value of power from the three analytical methods.

Method	Power (μW)
Experimental	7.44
Pin-force	32.5 – 172
Enhanced Pin-force	32.4 – 172
Euler Bernoulli	6.90 – 41.2

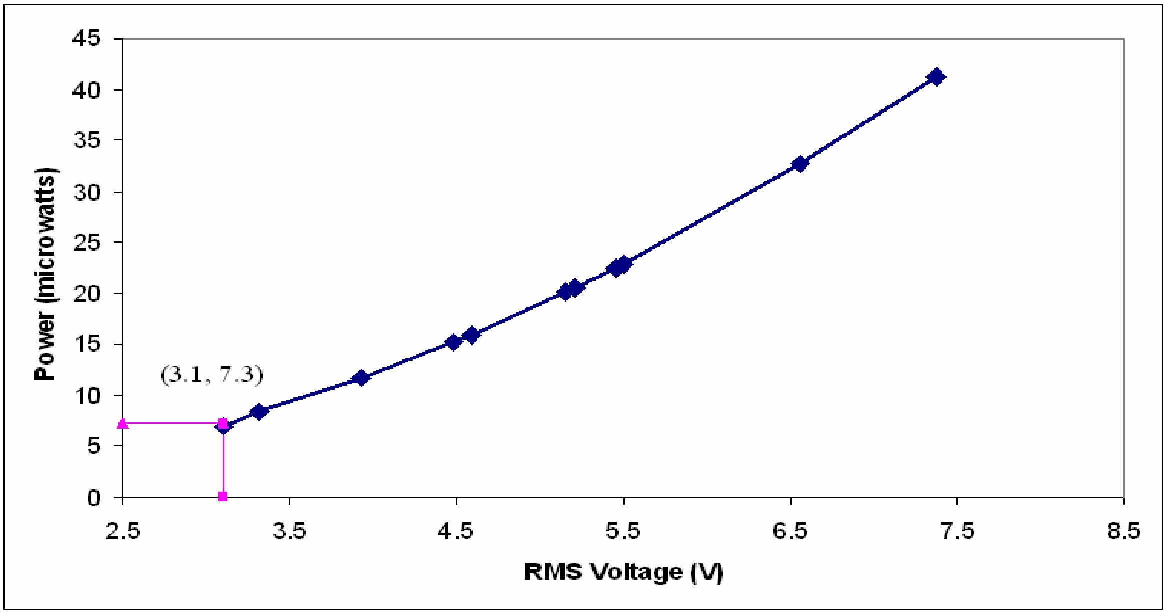

Figure 4.7. Trend-line for analytical power values generated by the random noise force.

Conclusions

The analytical model accurately simulates the forcing function and deflection values of a cantilever beam. The model using the Euler Bernoulli method accurately predicts voltage and power values of a cantilever beam excited by a harmonic forcing function or random noise. However, the models using the Pin-force and Enhanced pin-force methods overestimate the voltage and power values, and are not good indicators of experiment performance.

Some care must be taken to understand that the content of a random noise forcing function changes with every occurrence. To validate the analytical model when the beam is excited by a random noise force, the experimental power value must fall within the possible range of analytical power values. This is the case for the analytical beam model; thus, the Euler Bernoulli method can be used to reasonably model experimental results.

4.3 Cantilever plate experiment and comparison

This section will discuss the cantilever plate experiments and compare their results to the analytical models developed in Mathematica and MATLAB. First, the experimental procedure will be presented. The experiment will then be run with the harmonic forcing function. Comparisons of forcing function, voltage, and power values will be performed. This process will then be repeated for the random noise external forcing function.

4.3.1 Experimental procedure

The experimental procedure for the cantilever plate follows the procedure for the cantilever beam discussed in section 4.2.1. There are several minor changes which will be discussed. Figure 4.8 shows the cantilever plate setup. The plate's length, width, and thickness are defined as the plate's distance in the *x*-, *y*-, and *z*-directions, respectively.

The plate's dimensions are $63x40x0.9mm$. In order to be accurately modeled as a beam using the Euler Bernoulli beam method (which should not be confused with the piezoelectric modeling method), the structure's length should be at least ten times greater than its width. With slender, long beams, torsion is not a factor, but with a length less than ten times the width, torsion contributes to the structure deflection. The PZT covers the entire surface area of the top side of the plate. The PZT thickness is $0.2667mm$.

The forcing function is applied to the plate on the free tip as shown in Figure 2.10. This is to assure that the subsequent moment will be applied to the entire length of the PZT. The other change that is different from the beam procedure is that a combined Young's Modulus will be used. The PZT covers the one entire surface of the plate, thus adding stiffness which cannot be ignored. The combined modulus is calculated using equation (2.40) and is $68.943\times10^{9}\,Pa$. The combined thickness of the plate and PZT will be used as the plate thickness when calculating the natural frequencies and mode shapes.

There is a possible caveat when using the combined thickness. The total thickness of the system now becomes the plate thickness plus the PZT thickness. This causes a disparity when calculating the Pin-force method. The Pin-force method assumes that the strain applied to the plate increases linearly through the thickness of the plate but remains constant through the PZT. Since the PZT is assumed to be part of the plate, the strain increases through the PZT and the Pin-force method essentially becomes invalid. The Enhanced pin-force method assumes the strain increases linearly through the PZT also, so this method is still valid. However, within the equations for all three methods, there are several ratios given in equations (2.12) and (2.18). These ratios are of substrate thickness to PZT thickness. In the following sections for the plate model, in terms of these two ratios, Ψ and T, the substrate thickness is the original plate thickness only.

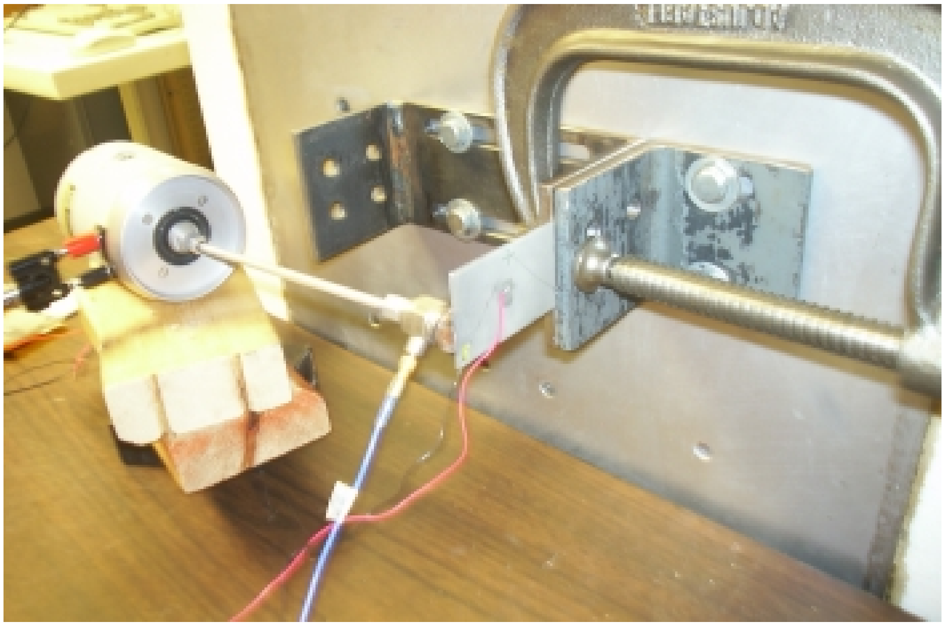

Figure 4.8. Experimental setup of plate.

4.3.2 Experimental plate results and comparison to analytical model

This section will discuss the experimental plate results and comparison to the analytical model. The forcing function will first be harmonic then changed to contain random noise content. After the data was collected, MATLAB is used to process the resulting signals.

<u>Plate with a harmonic driving force</u>

A comparison of the analytical model of the plate will be made to the experimental results. The input voltage signal produced by Siglab and sent to the shaker is given by

$$F(t) = 0.5\sin\left(2\pi\left(202.794\right)t\right) \tag{4.3}$$

where, the first resonant frequency of the plate is $202.794Hz$. Figure 4.9 shows the measured harmonic forcing function compared to analytical forcing functions. The analytical force with the magnitude of 0.4 matches the measured force more closely.

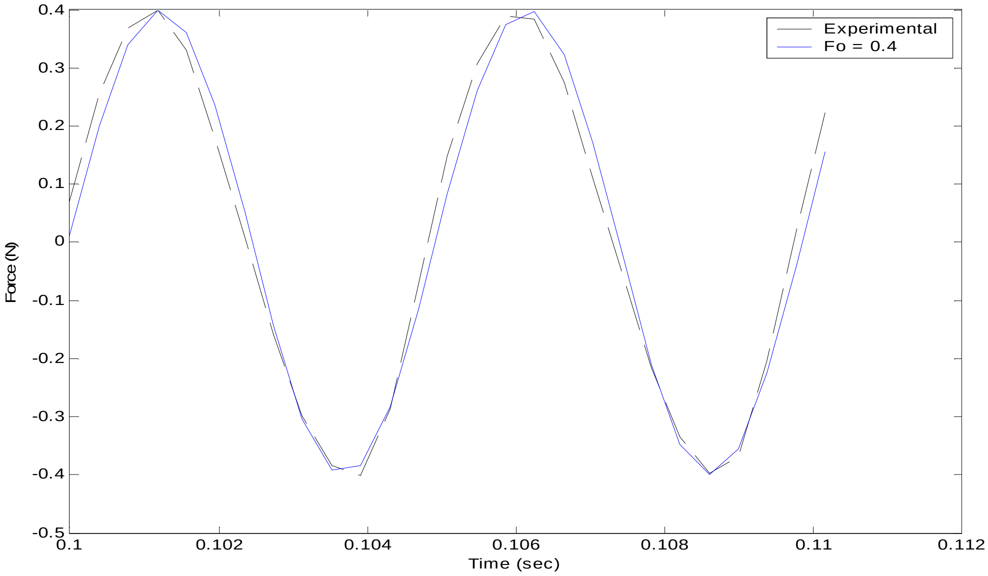

Figure 4.9. The measured harmonic force exerted on the plate is compared to analytical forcing function with a magnitude of 0.4*N*.

Next to be compared are the steady-state responses of the voltages. Figure 4.10 shows the experimental voltage and the voltage signal produced by the Euler Bernoulli method. This time the Euler Bernoulli method, with an amplitude of $105mV$, does not accurately predict the measured voltage signal, which has an amplitude of $80mV$. The Pin-force and Enhanced pin-force methods, which are not shown, produce very large amplitudes, of $1.1V$ and $0.95V$, respectively.

Lastly, the most important parameter, power, is examined. The power produced by the three analytical methods and the experiment are shown in Table 4.4. None of the three methods accurately predicts the experimental power value. The Pin-force and the Enhanced pin-force method both extremely overestimate the experimental power by two orders of magnitude. The Euler Bernoulli method produces a power which is 52% larger than the actual measured power. The three methods fail to accurately model a plate excited by a harmonic forcing function.

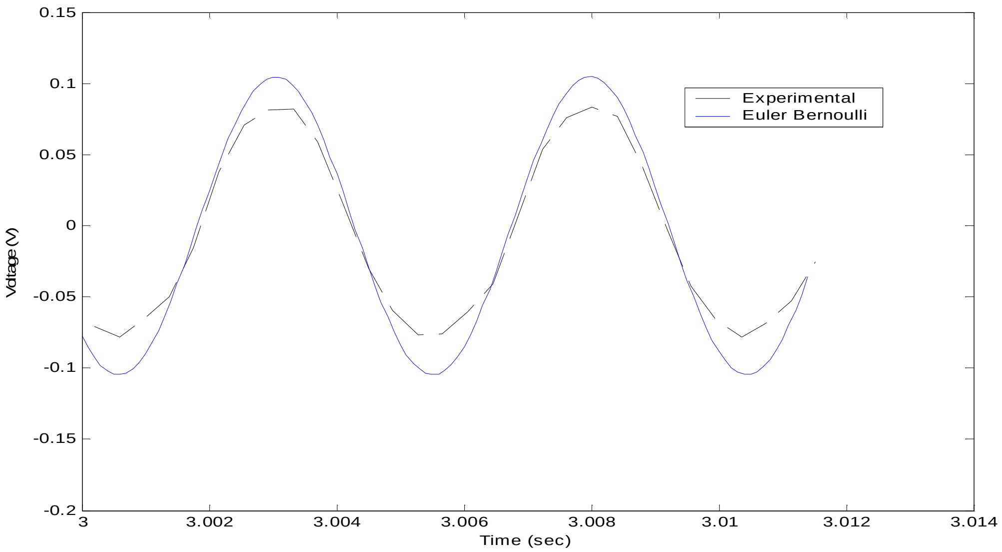

Figure 4.10. Experimental voltage compared to the Euler Bernoulli method voltage signals.

Table 4.4. Experimental power compared to the three analytical powers generated when excited by a harmonic forcing function.

Method	*Power* (μW)
Experimental	0.23
Pin-force	35.9
Enhanced Pin-force	28.8
Euler Bernoulli	0.35

Plate with a random noise driving force

The plate will now be excited by a random noise force, and the results compared. A frequency range of $0-1000Hz$ will be used with an RMS voltage value of $0.5V$. This range will enable the plate's first two resonant frequencies to possibly be excited. Figure 4.11 shows the experimental and analytical forces, respectively. The analytical force has amplitudes that are similar in magnitude to the experimental force.

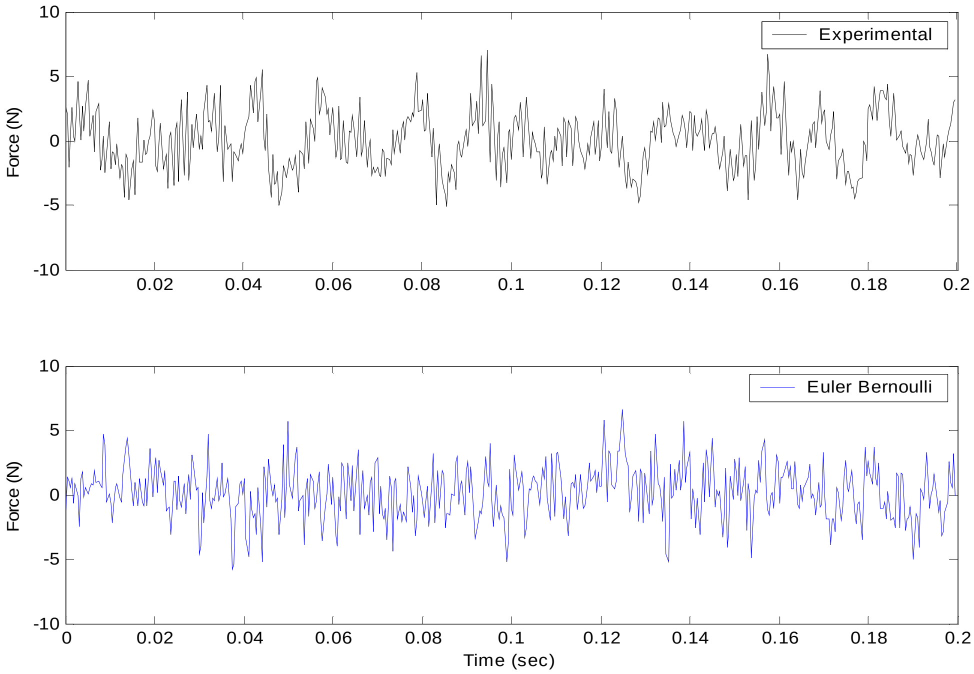

Figure 4.11. Experimental force measured by force transducer is compared to the analytical force generated.

Next the voltages are compared. The voltage signals generated from the random noise force are shown in Figure 4.12. Again, the Pin-force method and Enhanced pin-force method are not shown because they have been proven not to be good predictors of experimental data. The magnitudes are similar for the two signals. The Euler Bernoulli method produces a voltage signal with similar magnitudes compared to the experimental voltage signal. Some variation is expected due to the random nature of the forcing function. The RMS voltage for the experiment and for the three methods are calculated and shown in Table 4.5. The V_{RMS} value calculated by using the Euler Bernoulli method is roughly twice as large than the voltage measured experimentally. The Euler Bernoulli method produces a voltage signal that contains more low frequency content than the experimental voltage shown in Figure 4.12. This would cause the analytical voltage to have a higher RMS voltage.

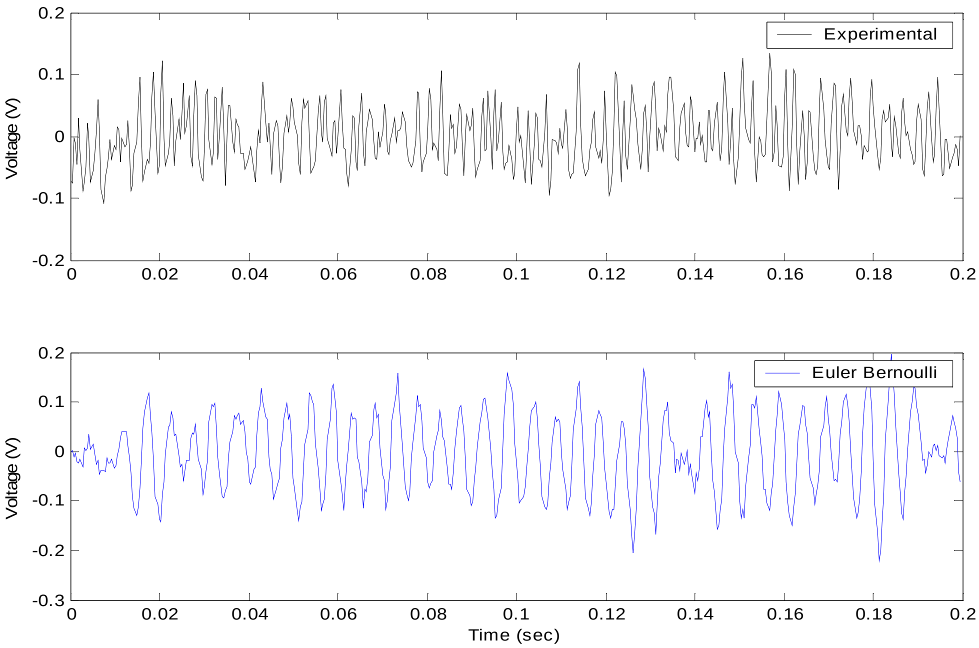

Figure 4.12. Experimental and analytical voltage signals generated from a PZT excited by a random noise force.

Table 4.5. Experimental voltage compared to an average value of voltage from the three analytical methods.

Method	Voltage (mV)
Experimental	47.2
Pin-force	892
Enhanced Pin-force	799
Euler Bernoulli	87.9

Lastly, the power values will be compared. The experimental power value is shown with three average power values of the analytical models in Table 4.6. All three analytical models overestimate the output power. The Euler Bernoulli method predicts a power value of $0.423\mu W$ which is almost three times larger than the measured power value.

Table 4.6. Power generated by a random excitation force on a plate.

Method	Power (μW)
Experimental	0.143
Pin-force	43.65
Enhanced Pin-force	35.01
Euler Bernoulli	0.423

Effects of damping ratio on Output Power Values

The purpose of this research is to quickly and accurately calculate an estimation of power generation of two different kinds of structures—beams and plates. Up to this point the damping ratio for both the beam and plate was chosen to be 0.03. If the damping ratio is unknown, it is not practical to experimentally confirm the damping ratio of a structure before using the models developed in this research. To confirm a damping ratio value, the structure must be setup for measurements to be taken. If the structure is already setup, it would be beneficial to proceed and calculate the output power experimentally, rather than predict it analytically.

Because the predicted output power from the plate analytical model is too large, the damping ratio is increased which will suppress deflections and lower the voltage and output power. Figure 4.13 shows the experimental voltage compared to the resulting voltage produced by the Euler Bernoulli method when the damping ratio value is 0.037. The Euler Bernoulli method accurately predicts the experimental voltage of the plate. The Pin-force method and Enhanced pin-force method again greatly overestimate the measured voltage and are not included in the graph. Table 4.7 compares the experimental power value to the analytical power value predicted by the Euler Bernoulli method. The Euler Bernoulli output power value is now a much better estimate than the power value calculated using the damping ratio of 0.03. The analytical model predicts the output power within $3nW$ of the measured output power which is only a 1% error.

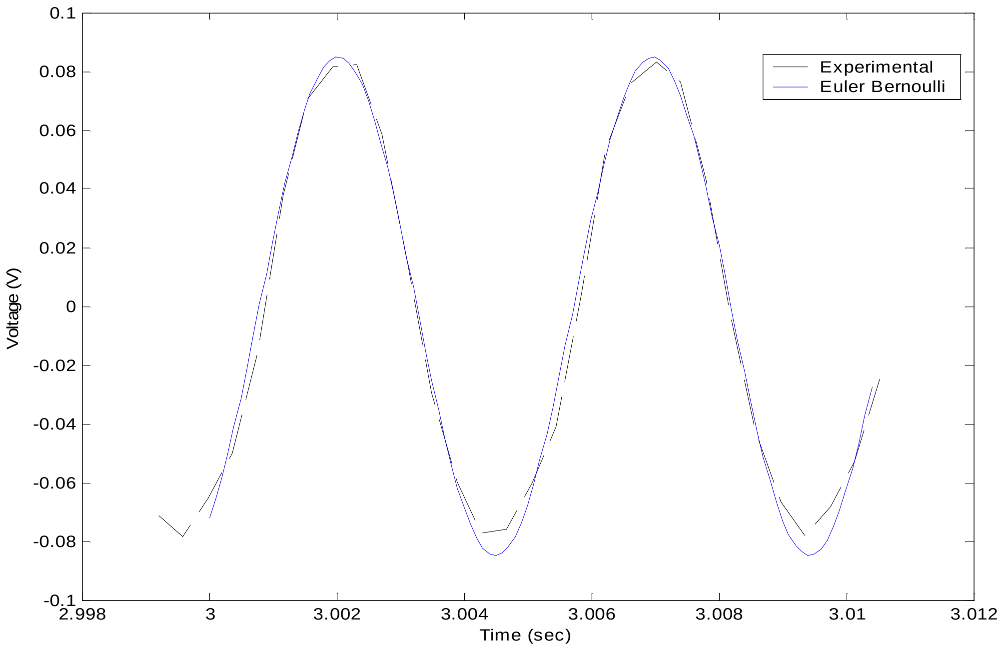

Figure 4.13. With a damping ratio of 0.037, the Euler Bernoulli method accurately predicts the experimental voltage of the plate.

Table 4.7. Output power from experiment and Euler Bernoulli method with $\zeta = 0.037$.

Method	Power (μW)
Experimental	0.227
Euler Bernoulli	0.230

Now, the change in damping ratio will be applied to the case where the plate is excited by a random noise force. The RMS voltage from the Euler Bernoulli method is compared with the measured RMS voltage in Table 4.8. An average RMS voltage value predicted by the analytical model using the Euler Bernoulli method is equivalent to the measured RMS voltage value.

Table 4.8. RMS voltage from a plate excited by a random noise force with $\zeta = 0.037$.

Method	V_{RMS} (mV)
Experimental	47.2
Euler Bernoulli	47.1

Finally, the output power generated from a random noise force will be examined. By increasing the damping ratio from 0.03 to 0.037, the range of possible output power values predicted by the Euler Bernoulli method is $40nW$ to $570nW$. By interpolation, as seen in Figure 4.14, a voltage value of $47mV$ corresponds to an analytical power value of $145nW$, which is only a 1% error. For this reason, the analytical model is reasonably accurate when predict output power.

Table 4.9. Output power from a plate excited by a random noise force with $\zeta = 0.037$.

Method	Power (nW)
Experimental	143
Euler Bernoulli	40 -- 570

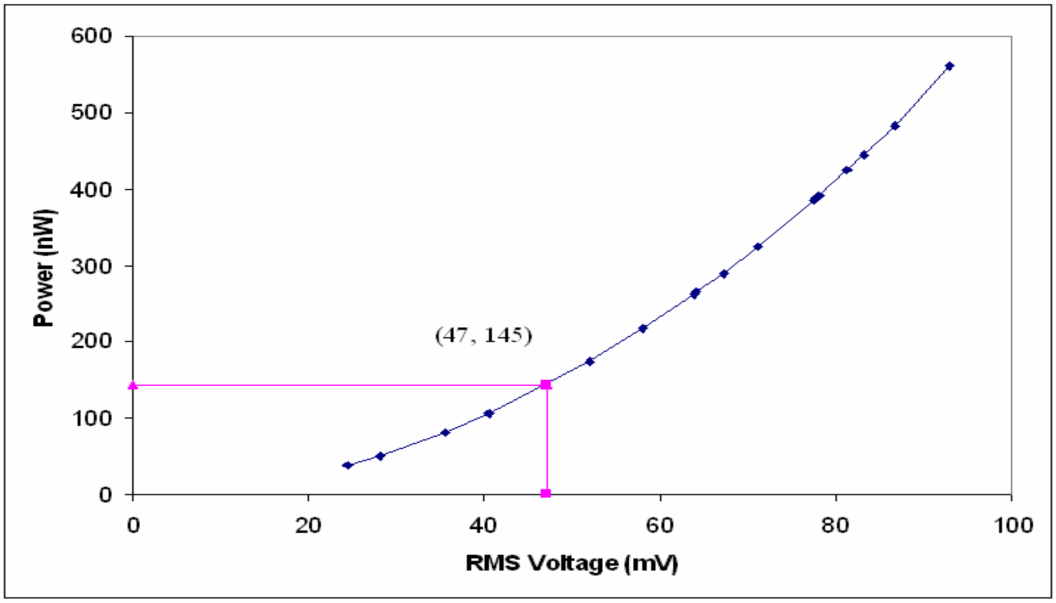

Figure 4.14. Trend-line for analytical power values generated by the random noise force.

4.4 Conclusions

The analytical beam model using the Euler Bernoulli method accurately predicts experimental power values for both a harmonic and random noise excitation force. The method closely matches the force and deflection signals. For the harmonic excitation force, the error in voltage values was only 1%. The error in power values is slightly greater at 8%. For the random noise force, the voltage error through interpolation was 1%. The analytical model is capable of generating a random force which will produce values close to the measured power.

The three analytical models fail to hold true for the plate model with a damping ratio of 0.03. For the harmonic forcing function, the force matches closely. For the harmonicly driven case, the Euler Bernoulli method predicts an output power value which is 52% higher than the actual measured power value. For the randomly driven case, the Euler Bernoulli method also overestimates the power generated by almost 300%. These errors are too high to be considered reliable.

When the damping ratio is changed to 0.037, the Euler Bernoulli method accurately predicts the output power. To ensure accurate results, the damping ratio should be known or estimated prior to attempting to predict the power produced by a certain system. The damping ratio directly affects the voltage and power. With the damping ratio of 0.037, the Euler Bernoulli method produces an output power with only a 1% error, compared to an error of 52% when the damping ratio is 0.03. For a plate excited by a random noise force, the analytical model using the Euler Bernoulli method is accurate by predicting a power value through interpolation that has only a 1% error.

Chapter 5

Conclusions

Analytical models that attempt to predict power generation from externally excited beam and plate structures have been developed and examined. From the analysis performed in this research, the following conclusions are made:

- An analytical model that predicts power generation from a vibrating beam has been developed. The model uses the Euler Bernoulli method to estimate the character of piezoelectric elements. The model accurately predicts deflection, voltage, and power generation from a beam that is excited by a harmonic force or random noise. Ideally, the force used to excite the beam could be arbitrary in nature.
- The analytical model developed here has been shown to hold true when predicting power generation from plates excited by the first harmonic frequency and by random noise vibrations. To obtain accurate estimations of power generation, the damping ratio should be well estimated.
- A parametric study was performed to maximize power output for the beam structure. The piezoelectric element's location was determined to be optimal adjacent to the clamped end. The piezoelectric element's length was determined to be optimal at $0.300m$ on a beam with a length of $0.550m$. For the Euler Bernoulli method, the thickness ratio was optimized at 0.525. Finally, the transverse forcing function location was determined to be optimal at the free end of a cantilever beam, producing the largest moment arm.
- The analysis of the three piezoelectric modeling methods determined that the Euler Bernoulli method better estimates the behavior of a piezoelectric element used for designing a power harvesting system. Though the Pin-force and

Enhanced pin-force methods are simpler in nature, they fail to take under consideration the constant bonding between the piezoelectric element and the substrate and a need for a new neutral bending axis. These effects are significant when computing the power generated from a piezoceramic wafer.

- Damping plays a critical role when predicting power from PZT wafers. Ideally, the damping ratio would be known to ensure precise and accurate results. Oftentimes, a way of determining the damping ratio involves performing log decrement analyses or frequency response calculations. The purpose of this research is to develop analytical models to eliminate the need for laboratory experiments and quickly predict power generated from certain systems.

Recommendations for Future Work

From the experience of this research, the following recommendations on future work are suggested:

- A continuation of this analytical model can be performed that predicts the power generation for any arbitrary forcing function can be established. An impact force or a force that is turned on and off, are forces that also exist in industry and could have an impact on power generation capabilities.
- An accurate method of estimating damping ratio for these analytical models should be investigated. Damping ratio for a structure needs to be well estimated before using the models to predict power generation.
- An interactive, user-interface in the software code that would allow the user to input dimensions, parameters, and properties of a system. This would allow easy use for someone who is not accustomed to the particular software code and could eliminate possible input errors by directly changing the software code.
- An analytical model that properly predicts power generation for an arbitrary substrate shape can be established. Plates, disks, membranes, and toruses are all shapes that are used in industry and that could provide a base for power generation.

- The storage of the generated power should be examined. Storing a charge in a capacitor or recharging a battery are plausible options.
- Applications for the use of the generated power can be determined. Though the generated power is low in magnitude, if stored over time, the power can be used intermittently.

Bibliography

Allen, J. and Smits, A. *Energy Harvesting Eel.* **Journal of Fluids and Structures,** Vol.15, 2001, pp.1-13.

Amirtharajah, R., Chandrakasan, A. P. *Self-powered Signal Processing Using Vibration-based Power Generation.* **IEEE journal of solid-state circuits**, Vol. 33, No. 5, May 1998, pp. 687-695.

Amirtharajah, R. and Chandrakasan, A. *Self-powered Low Power Signal Processing*. 1997 Symposium on VLSI circuits digest of technical papers.

Beer, F. P. and Johnston, Jr., E. R. **Mechanics of Materials,** 2nd Ed, McGraw-Hill, Inc., New York, 1992.

Blevins, R. D. *Formulas for Natural Frequency and Mode Shape*. 4th Edition, Robert E. Krieger Publishing Co., Florida. 1987, p.254.

Crawley, E. F., de Luis, J. *Use of Piezoelectric Actuators as Elements of Intelligent Structures.* Present as Paper 86-0878 at the AIAA/ASME/ASCE/AHS Active Structures, Structural Dynamics and Materials Conference, San Antonio, TX, May 19-21, 1986.

Dimitriadis, E. K., Fuller, C. R., and Rogers, C. A. *Piezoelectric Actuators for Distributed Vibration Excitation of Thin Plates.* **Journal of Vibrations and Acoustics,** Vol. 113, January 1991, pp.100-107.

Dosch, J. J., Inman, D. J., Garcia, E. *A Self-sensing Piezoelectric Actuator for Collocated Control.* **Journal of Intelligent Material Systems and Structures**, Vol. 3, January 1992, pp.166-185.

Elvin, N. G., Elvin, A. A., and Spector, Myron. *A Self-powered Mechanical Strain Energy Sensor.* **Smart Materials and Structures**, Vol. 10, 2001, pp.293-299.

Gao, J. X., Shen, Y. P., and Wang, J. *Three Dimensional Analysis for Free Vibration of Rectangular Composite Laminates with Piezoelectric Layers.* **Journal of Sound and Vibration**, Vol. 213, No. 2, 1998, pp. 383-390.

Gonzalez, J., Rubio, A., and Moll, F. *A Prospect on the Use of Piezoelectric Effect to Supply Power to Wearable Electronic Devices.*

Goldfarb, M. Hones, L.D., 1997. *A Lumped Parameter Electromechanical Model for Describing the Nonlinear Behavior of Piezoelectric Actuators*. **ASME Journal of Dynamic systems, measurement, and control**, Vol.119, No. 3, pp.478-485.

Hambley, A. Electrical Engineering, Prentice Hall, 1997.

Hausler, E. and Stein, L. *Implantable Physiological Power Supply with PVDF Film.* **Ferroelectronics**, Vol. 60, 1984, pp. 277-282.

He, S. Y., Chen, W. S., Chen, Z. L. *A Uniformizing Method for the Free Vibration Analysis of Metal-Piezoceramic Composite Thin Plates.* **Journal of Sound and Vibration,** Vol. 217, No. 2, 1998, pp. 261-281.

Heyliger P. R. *Exact Solutions for Simply-Supported Laminated Piezoelectric Plates,* **Journal of Applied Mechanics,** Vol. 64, No. 2, 1997, pp. 299-306

Hofmann, H., Ottman, G. K., and Lesieutre, G. A. *Optimized Piezoelectric Energy Harvesting Circuit Using Step-Down Converter in Discontinuous Conduction Mode.* 33rd Annual IEEE Power Electronics Specialists Conference, Cairns Convention Centre, Queensland, Australia. June 2002, pp. 1-14.

Ikeda, T. **Fundamentals in Piezoelectricity**, Oxford Press, Oxford, 1990.

Inman, D. J. **Engineering Vibration**, 2nd edition, Prentice Hall, 2000.

Inman, D. J., and Cudney, H. H. *Structural and Machine Design Using Piezoceramic Materials: A Guide for Structural Design Engineers.* Final Report to NASA Langley Research Center, April 30, 2000.

Jaffe, B., Roth, R. S., and Marzullo, S. *Piezoelectric Properties of Lead Zirconate-Lead Titanate Solid-Solution Ceramics.* **Journal of Applied Physics**, Vol. 6, No. 25, 1954, pp.809-810.

Kasyap, A., et al. *Energy Reclamation from a Vibrating Piezoceramic Composite Beam.* Ninth International Congress on Sound and Vibration, ICSV9.

Kendall, C. J. *Parasitic Power Collection in Shoe Mounted Devices.* Submitted to the Dept. of Physics for fulfillments in Bachelor of Science, Massachusetts Institute of Technology, June 1998.

Kulkarni, G., and Hanagud, S. V. *Modeling Issues in the Vibration Control with Piezoceramix Actuators.* **Smart Structures and Materials,** AD-Vol. 24/AMD-Vol. 123, 1991, pp.7-13.

Kymissis, J., Kendall, C., Paradiso, J., Gershenfeld, N. *Parasitic Power Harvesting in shoes.* Presented at the second IEEE International conference on wearable computing. Draft 2.0, August 1999.

Lakic. *Inflatable Boot Liner with Electrical Generator and Heater*. Patent No. 4845338, 1989.

Lesieutre, G. A., Hofmann, H. F., and Ottman, G. K. *Structural Damping Due to Piezoelectric Energy Harvesting.*

Lui, G. R., Peng, X. Q., Lam, K. Y. *Vibration Control Simulation of Laminated Composite Plates with Integrated Piezoelectrics.* **Journal of Sound and Vibration,** Vol. 220, No. 5, 1999, pp. 827-846.

Ottman, G. K., Hofmann, H., Bhatt, A. C., and Lesieutre, G. A. *Adaptive Piezoelectric Energy Harvesting Circuit for Wireless, Remote Power Supply.* IEEE Transactions on Power Electronics, Vol. 17, No. 5, September 2002, pp.1-8.

Park, G. Memorandum based upon Kaihong paper, Center for Intelligent Material Systems and Structures, Virginia Polytechnic Institute and State University, 2001.

Ready, J. N. *Mechanics of Laminated Composite Plates: Theory and Analysis*. CRC Press, Inc., 1997, p.140.

Rizzoni, G. *Principles and Applications of Electrical Engineering*, 3rd Ed., McGraw-Hill, 2001.

Sirohi, J., and Chopra, I. *Fundamental Understanding of Piezoelectric Strain Sensors.* **Journal of Intelligent Material Systems and Structures**, Vol. 11, April 2000, pp.246-257.

Smits, J., and Choi, W. *The Constituent Equations of Piezoelectric Heterogeneous Bimorphs.* **IEEE Transactions on Ultrasonics, Ferroelectrics, and Frequency Control,** Vol. 38, May 1991, pp.256-270.

Sodano, H., Magliula, E. A., Park, G., and Inman, D. J. *Electric Power Generation using Piezoelectric Devices.* 13th International Conference on Adaptive Structure and Technologies, 2002.

Starner, T. *Human-powered Wearable Computing.* **IBM Systems Journal**, Vol. 35, Nos. 3 & 4, 1996, pp.618-629.

Umeda, M., Nakamura, K., and Ueha, S. *Energy Storage Characteristics of a Piezo-generator Using Impact Vibration.* **Japan Journal of Applied Physics**, Vol. 36, Part 1, No. 5b, May 1997, pp.3146-3151.

Umeda, M., Nakamura, K., Ueha, S. *Analysis of the Transformation of Mechanical Impact Energy to Electric Energy Using Piezoelectric Vibrator.*

Wang, K. *Modeling of Piezoelectric Generator on a Vibrating Beam.* For completion of Class Project in ME 5984 Smart Materials, Virginia Polytechnic Institute and State University, April 2001.

Wang, X., Ehlers, C., and Neitzel, M. *An analytical investigation of static models of piezoelectric patches attached to beams and plates.* **Smart Materials and Structures**, Vol. 6, 1997, pp.204-213.

Williams, C.B., Yates, R.B. *Analysis of a Micro-electric Generator for Microsystems*. 8th International Conference on Solid-state Sensors and Actuators, and Eurosensors. Stockholm, Sweden, June 1995, pp.369-372.

Young, D. *Vibration of Rectangular Plates by the Ritz Method*. **Journal of Applied Mechanics**, December 1950, pp.448-453.

Appendix A

Analytical model code for beam

Harmonic input analytical model for beam

```
clear all;
close all;
```

Beam properties and dimensions

```
rho = 2715;                          %kg/m^3      density
Ebeam  = 71e9;                      %Pa            Young's modulus
Lbeam  = .558;                      %m             length
width  = .050;                      %m             beam width
thickbeam  = .004;                  %m             thickness
Lf  = .200;                         %m    length to forcing f(t)
Area  = thickbeam*width;            %m^2  Area
I   = width*thickbeam^3/12;         %m^4  M. A. of inertia
c   = (Ebeam*I/(rho*Area))^.5;
%piezo properties
g31 = -9.5e-3;                       %V*m/N  voltage constant
Epiezo = 62e9;                       %Pa    Young's Modulus
thickpiezo = .508e-3;                %m     thickness
Lpiezo = .073;                       %m     length
d31 = -320e-12;                      %m/volt dielectric constant
Rsource = 330000;                    %ohm    source resistance
```

Natural frequencies of the beam for a clamped-free beam

```
B = 0:.01:50;                       %(wn/c)^2;
cheq = cos(Lbeam*B).*cosh(Lbeam*B);
plot(B,cheq)
axis([0 30 -5 5])
hold on;
ezplot('-1',[0 30 -5 5])
axis([0 30 -5 5])
xlabel('Beta values');title('Graph of Characteristic equation')
beta = [3.3604;8.4123;14.0766;19.71;25.335];
wn = beta.^2*c;
fn = wn/(2*pi);
```

Mode shapes

```
syms x
for i=1:5,
   ModeShape(i) = cosh(beta(i)*x)-cos(beta(i)*x)-(sinh(beta(i)*Lbeam)...
      -sin(beta(i)*Lbeam))/(cosh(beta(i)*Lbeam)+cos(beta(i)*Lbeam))...
      *(sinh(beta(i)*x)-sin(beta(i)*x));
end
```

Harmonic forcing function

```
w = wn;
```

```
zeta = .03;
wd = wn*(1-zeta^2)^.5;
syms t tt
Force = (.35)*sin(w(1)*tt)*1/(rho*Area)*subs(ModeShape,x,Lf);
for i=1:5
   q(i) =  1/wd(i)*exp(-zeta*wn(i)*t)...
   *int(Force(i)*exp(zeta*wn(i)*tt)*sin(wd(i)*(t-tt)),tt,0,t);
end
```

Develop equations for deflection and equations for voltage

```
for i=1:5
   before_w3(i) = q(i)*ModeShape(i);
end
w3 = sum(before_w3);
K_x_t = vpa(diff(w3,x,2),5);
Kavg = vpa((1/Lpiezo)*int(K_x_t,x,0,Lpiezo),5);
tau = 2:.01:5;
Moment = Ebeam*I.*Kavg;

psi = (Ebeam*thickbeam)/(Epiezo*thickpiezo);
Vpinforce_sym = (6*g31)/(width*thickbeam*(3-psi)).*Moment;
Vpinforce = subs(Vpinforce_sym,'t',tau);
T = thickbeam/thickpiezo;
Venhanced_sym = (6*g31*T)/(width*thickpiezo*(3*T^2-1-psi*T^2)).*Moment;
Venhanced = subs(Venhanced_sym,'t',tau);
Veb_sym= (6*g31*psi*(1+T))/(width*thickpiezo*(1+psi^2*T^2+2
     *psi*(2+3*T+2*T^2))).*Moment;
Veb = subs(Veb_sym,'t',tau);
```

Calculate maximum power

```
Ppinforce_i = [];
Penhanced_i = [];
Peb_i = [];
Rload = 1000:1000:1e6;
for RL = 1000:1000:1e6
   Ppinforce = (mean(Vpinforce.^2)*(RL/(RL+Rsource)^2));    %the root part of RMS
cancels out with the subsequent ^2 term when calc'ing power = V^2/R
   Penhanced = (mean(Venhanced.^2)*(RL/(RL+Rsource)^2));
   Peb = (mean(Veb.^2)*(RL/(RL+Rsource)^2));

   Ppinforce_i = [Ppinforce_i Ppinforce];
   Penhanced_i = [Penhanced_i Penhanced];
   Peb_i = [Peb_i Peb];
end
plot(Rload,Ppinforce_i);
hold on;
```

```
plot(Rload,Penhanced_i,'r');
plot(Rload,Peb_i,'g');
Power_pinforce = max(Ppinforce_i)
Power_Penhanced = max(Penhanced_i)
Power_Peb = max(Peb_i)
```

Random Noise input analytical model for beam

Random noise force
(all else the same as harmonic input code)

```
Force_i = 0;
freqrange = 100*2*pi;
for i=1:50
    oneForce = (0.35)*sin(rand(1)*freqrange*tt-rand(1)*2*pi);
    Force_i = Force_i + oneForce;
end
Force = Force_i*1/(rho*Area)*subs(ModeShape,x,Lf);

for i=1:5
    q(i) =  1/wd(i)*exp(-.03*wn(i)*t)...
    *int(Force(i)*exp(.03*wn(i)*tt)*sin(wd(i)*(t-tt)),tt,0,t);
end
```

Appendix B

Analytical model code for plate

Harmonic input analytical model for plate

Mathematica

Plate physical constants

```
<< LinearAlgebra`MatrixManipulation`
<< Graphics`Legend`
Off[General::spell1]
a = 0.063;(*m*)
b = 0.04;
Estiff = 68.943*10^9; (*Pa*)
ν = 0.3;
ρAL = 2715; (*kg/m^3*)
thickAL = .9*10^-3; (*m*)
ρPZT = 7800; (*kg/m^3*)
thickPZT = .2667*10^-3; (*m*)
thick = thickAL + thickPZT;
m1 = ρAL*thickAL + ρPZT*thickPZT;
Dstiff = (Estiff*thick^3)/(12*(1 - ν^2));
Λ = (ω^2*m1*a^3*b)/Dstiff;
M = 2;
NN = 3;
(*Sqrt[Dstiff/(ρ*thick*a^4)]*)
```

Define constants for clamped-free beam in X direction and for Free-Free beam in Y direction

```
λ[1] = 1.8751041; λ[2] = 4.6940911; λ[3] = 7.8547574; λ[4] = 10.9955407;
λ[5] = 14.1371684; λ[6] = (2*6 - 1)*π/2; λ[7] = (2*7 - 1)*π/2;
λ[8] = (2*8 - 1)*π/2; λ[9] = (2*9 - 1)*π/2;
α[1] = 0.7340955; α[2] = 1.01846644; α[3] = 0.99922450; α[4] = 1.00003355;
α[5] = 0.99999855; α[6] = 1; α[7] = 1; α[8] = 1;
α[9] = 1;
μ[1] = 0; μ[2] = 0; μ[3] = 4.7300408; μ[4] = 7.8532046; μ[5] = 10.9956078;
μ[6] = 14.1371655; μ[7] = 17.2787596; μ[8] = (2*8 - 3)*π/2; μ[9] = (2*9 - 3)*π/2;
β[3] = 0.98250222; β[4] = 1.00077731; β[5] = 0.99996645;
β[6] = 1.00000145;
```

Mode shapes

```
Do[X[r][x_] = Cosh[λ[r] * x / a] - Cos[λ[r] * x / a] - α[r] * (Sinh[λ[r] * x / a] - Sin[λ[r] * x / a]),
 {r, 1, M * NN}]
Y[1][y_] = 1;
Y[2][y_] = √3 * (1 - 2 * y / b);
Do[Y[r][y_] = Cosh[μ[r] * y / b] + Cos[μ[r] * y / b] - β[r] * (Sinh[μ[r] * y / b] + Sin[μ[r] * y / b]),
 {r, 3, M * NN}]
(*Do[Print[X[r][x]],{r,1,M*NN}]*)
(*Do[Print[Y[r][y]],{r,1,M*NN}]*)
U3[1][x_, y_] = X[1][x] * Y[1][y];
U3[2][x_, y_] = X[1][x] * Y[2][y];
U3[3][x_, y_] = X[2][x] * Y[1][y];
U3[4][x_, y_] = X[2][x] * Y[2][y];
U3[5][x_, y_] = X[1][x] * Y[3][y];
```

“Convenient Integrals”

```
Eimeq[i_, m_] = a * ∫_0^a X[i][x] * D[X[m][x], {x, 2}] ⅆx;
Emieq[m_, i_] = a * ∫_0^a X[m][x] * D[X[i][x], {x, 2}] ⅆx;
Fkneq[k_, n_] = b * ∫_0^b Y[k][y] * D[Y[n][y], {y, 2}] ⅆy;
Fnkeq[n_, k_] = b * ∫_0^b Y[n][y] * D[Y[k][y], {y, 2}] ⅆy;
Himeq[i_, m_] = a * ∫_0^a D[X[i][x], {x, 1}] * D[X[m][x], {x, 1}] ⅆx;
Kkneq[k_, n_] = b * ∫_0^b D[Y[k][y], {y, 1}] * D[Y[n][y], {y, 1}] ⅆy;
Timing[Eim = Chop[Table[Eimeq[i, m], {i, 1, M * NN}, {m, 1, M * NN}]]];
Timing[Emi = Chop[Table[Emieq[m, i], {m, 1, M * NN}, {i, 1, M * NN}]]];
Timing[Fkn = Chop[Table[Fkneq[k, n], {k, 1, M * NN}, {n, 1, M * NN}], 10^-4]];
Timing[Fnk = Chop[Table[Fnkeq[n, k], {n, 1, M * NN}, {k, 1, M * NN}], 10^-4]];
Timing[Him = Chop[Table[Himeq[i, m ], {i, 1, M * NN}, {m, 1, M * NN}]]];
Timing[Kkn = Chop[Table[Kkneq[k, n], {k, 1, M * NN}, {n, 1, M * NN}], 10^-4]];
TableForm[Eim];
TableForm[Emi];
TableForm[Fkn];
TableForm[Fnk];
TableForm[Him];
TableForm[Kkn];
sys = ZeroMatrix[M * NN, M * NN];
ik = {{1, 1}, {1, 2}, {2, 1}, {2, 2}, {1, 3}, {2, 3}};
TableForm[ik];
```

```
tabl = ZeroMatrix[M * NN, M * NN];

tabl[[1, 1]] = tab[[1, 1, 1, 1]];
tabl[[1, 2]] = tab[[1, 1, 1, 2]];
tabl[[1, 3]] = tab[[1, 1, 1, 3]];
tabl[[1, 4]] = tab[[1, 1, 2, 1]];
tabl[[1, 5]] = tab[[1, 1, 2, 2]];
tabl[[1, 6]] = tab[[1, 1, 2, 3]];

tabl[[2, 1]] = tab[[1, 2, 1, 1]];
tabl[[2, 2]] = tab[[1, 2, 1, 2]];
tabl[[2, 3]] = tab[[1, 2, 1, 3]];
tabl[[2, 4]] = tab[[1, 2, 2, 1]];
tabl[[2, 5]] = tab[[1, 2, 2, 2]];
tabl[[2, 6]] = tab[[1, 2, 2, 3]];

tabl[[3, 1]] = tab[[1, 3, 1, 1]];
tabl[[3, 2]] = tab[[1, 3, 1, 2]];
tabl[[3, 3]] = tab[[1, 3, 1, 3]];
tabl[[3, 4]] = tab[[1, 3, 2, 1]];
tabl[[3, 5]] = tab[[1, 3, 2, 2]];
tabl[[3, 6]] = tab[[1, 3, 2, 3]];

tabl[[4, 1]] = tab[[2, 1, 1, 1]];
tabl[[4, 2]] = tab[[2, 1, 1, 2]];
tabl[[4, 3]] = tab[[2, 1, 1, 3]];
tabl[[4, 4]] = tab[[2, 1, 2, 1]];
tabl[[4, 5]] = tab[[2, 1, 2, 2]];
tabl[[4, 6]] = tab[[2, 1, 2, 3]];

tabl[[5, 1]] = tab[[2, 2, 1, 1]];
tabl[[5, 2]] = tab[[2, 2, 1, 2]];
tabl[[5, 3]] = tab[[2, 2, 1, 3]];
tabl[[5, 4]] = tab[[2, 2, 2, 1]];
tabl[[5, 5]] = tab[[2, 2, 2, 2]];
tabl[[5, 6]] = tab[[2, 2, 2, 3]];

tabl[[6, 1]] = tab[[2, 3, 1, 1]];
tabl[[6, 2]] = tab[[2, 3, 1, 2]];
tabl[[6, 3]] = tab[[2, 3, 1, 3]];
tabl[[6, 4]] = tab[[2, 3, 2, 1]];
tabl[[6, 5]] = tab[[2, 3, 2, 2]];
tabl[[6, 6]] = tab[[2, 3, 2, 3]];

MatrixForm[tabl];
```

```
For[r = 1, r ≤ M * NN, i = ik[[r, 1]]; k = ik[[r, 2]];
 tabl[[r, r]] =
  (b/a * λ[i]^4 + a^3/b^3 * μ[k]^4 + 2 * ν * a/b * Eim[[i, i]] * Fkn[[k, k]] +
    2 * (1 - ν) * a/b * Him[[i, i]] * Kkn[[k, k]] - Λ); r++]
MatrixForm[tabl];
```

Natural frequencies

```
omega = Solve[Det[tabl] == 0 /. ω -> √Ω, Ω];
Do[f[i] = √omega[[i, 1, 2]] / (2 * π), {i, 1, M * NN}]
Do[Print[f[i]], {i, 1, M * NN}]
Do[ωn[i] = 2 * π * f[i], {i, 1, 5}]
Do[Print[ωn[i]], {i, 1, 5}]
```

Harmonic Force input

```
ξ = .037;(*damping coeff*)
ωdr = ωn[1];
U3ab[1] = X[1][a] * Y[1][b / 2];
U3ab[2] = X[1][a] * Y[2][b / 2];
U3ab[3] = X[2][a] * Y[1][b / 2];
U3ab[4] = X[2][a] * Y[2][b / 2];
U3ab[5] = X[1][a] * Y[3][b / 2];
Do[Force[z][tt_] = .4 * Sin[ωdr * tt] * 1/m1 * U3ab[z], {z, 1, 5}]
Do[ωdamp[z] = ωn[z] * √(1 - ξ^2), {z, 1, 5}];
Do[
 q[z][t_] = 1/ωdamp[z] * ⅇ^(-ξ*ωn[z]*t) *
   ∫_0^t Force[z][tt] * ⅇ^(ξ*ωn[z]*tt) * Sin[ωdamp[z] * (t - tt)] ⅆtt, {z, 1, 5}];
(*Do[Print[q[z][t]],{z,1,5}]*)
```

Equation of deflection and curvature

```
w3[t_, x_, y_] = Chop[Simplify[Sum_{z=1}^{4} q[z][t] * U3[z][x, y]]];
κx[t_, x_] = Chop[Simplify[∂_{x,x} w3[t, x, y]]];
κeqn[t_, x_] = κx[t, x];
κavg[t_] = Chop[Simplify[1/a * ∫_0^a κeqn[t, x] ⅆx]];
MomentPlate[t_] = Chop[-Dstiff * b * κavg[t]] ;
```

Calculate voltage and power from the three methods

```
plot3 = Plot[Vpinforce[t], {t, 2, 2.01}, DisplayFunction → Identity,
   PlotStyle → RGBColor[1, 0, 0]];
plot4 = Plot[Venhanced[t], {t, 2, 2.01}, DisplayFunction → Identity,
  PlotStyle → RGBColor[0, 1, 0]]
plot5 = Plot[-Veb[t], {t, 2, 2.01}, DisplayFunction → Identity,
   PlotStyle → RGBColor[0, 0, 1]];
plot6 = ListPlot[{{2.0000 + .0005, -0.0434}, {2.0004 + .0005, -0.0020},
    {2.0008 + .0005, 0.0513}, {2.0012 + .0005, 0.0752}, {2.0016 + .0005, 0.0821},
    {2.0020 + .0005, 0.0781}, {2.0023 + .0005, 0.0503}, {2.0027 + .0005, 0.0026},
    {2.0031 + .0005, -0.0399}, {2.0035 + .0005, -0.0653}, {2.0039 + .0005, -0.0781},
    {2.0043 + .0005, -0.0700}, {2.0047 + .0005, -0.0543}, {2.0051 + .0005, -0.0311},
    {2.0055 + .0005, 0.0209}, {2.0059 + .0005, 0.0646}, {2.0063 + .0005, 0.0789},
    {2.0066 + .0005, 0.0831}, {2.0070 + .0005, 0.0706}, {2.0074 + .0005, 0.0333},
    {2.0078 + .0005, -0.0157}, {2.0082 + .0005, -0.0513}, {2.0086 + .0005, -0.0720},
    {2.0090 + .0005, -0.0774}, {2.0094 + .0005, -0.0638}, {2.0098 + .0005, -0.0480}},
   DisplayFunction → Identity, PlotJoined → True];
Show[{plot3, plot4, plot5, plot6}, DisplayFunction → $DisplayFunction,
  Frame → False, AxesLabel → {Time (sec), Voltage (V)}]
```

```
Rsource = 3900;
```

$$\text{Ppinforce}[\text{RL\_}] = \sum_{t=0}^{1000} \frac{\text{Vpinforce}[2 + t * .0001]^2}{1001} * \frac{\text{RL}}{(\text{RL} + \text{Rsource})^2};$$

$$\text{Penhanced}[\text{RL\_}] = \sum_{t=0}^{1000} \frac{\text{Venhanced}[2 + t * .0001]^2}{1001} * \frac{\text{RL}}{(\text{RL} + \text{Rsource})^2};$$

$$\text{Peb}[\text{RL\_}] = \sum_{t=0}^{1000} \frac{\text{Veb}[2 + t * .0001]^2}{1001} * \frac{\text{RL}}{(\text{RL} + \text{Rsource})^2};$$

```
Plot[{Ppinforce[RL], Penhanced[RL], Peb[RL]}, {RL, 0, 10000},
  AxesLabel → {Resistance (ohm), Power (W)},
  PlotStyle → {RGBColor[1, 0, 0], RGBColor[0, 1, 0], RGBColor[0, 0, 1]}];
Ppinforce[3900]
Penhanced[3900]
Peb[3900]
```

MATLAB

```
clear all;
close all;


format short g
a = 0.063;
b = 0.04;
Estiff = 68.943e9;
nu = 0.3;
```

```
rhoAL = 2715;
thickAL = 0.9e-3;
rhoPZT = 7800;
thickPZT = 0.2667e-3;
thick = thickAL + thickPZT;
m1 = rhoAL*thickAL + rhoPZT*thickPZT;
Dstiff = Estiff*thick^3/(12*(1-nu^2));


fn = [202.794;801.956;1052.01;2571.54;3728.7];
wn = [1274.19;5038.84;6609.97;16157.4;23428.1];
syms x y
X1 = -cos(29.763*x)+cosh(29.7636*x)-0.734096*(-sin(29.7637*x)...
   +sinh(29.7636*x));
X2 = -cos(74.5094*x)+cosh(74.5094*x)-1.01847*(-sin(74.5094*x)...
   +sinh(74.5094*x));
Y1 = 1;
Y2 = 3^.5*(1-50*y);
Y3 = cos(188.251*y)+cosh(118.251*y)...
   -0.982502*(sin(118.251*y)+sinh(118.251*y));

U3 = zeros(5,1);
U3 = sym(U3);
U3(1) = X1*Y1;
U3(2) = X1*Y2;
U3(3) = X2*Y1;
U3(4) = X2*Y2;
U3(5) = X1*Y3;
U3 = vpa(U3,6);

w = wn(1);
zeta = 0.037;
wdamp = wn*(1-zeta^2)^.5;
U3a = zeros(5,1);
U3a = vpa(subs(U3,'x',a),6);
U3ab = vpa(subs(U3a,'y',b/2),6);
U3ab(2) = 0;
U3ab(4) = 0;


syms t tt
Force = vpa(0.4*sin(w*tt)*1/m1*U3ab,6);
for z = 1:4,
   q(z) = 1/wdamp(z)*exp(-zeta*wn(z)*t)...
      *int(Force(z)*exp(zeta*wn(z)*tt)*sin(wdamp(z)*(t-tt)),tt,0,t);
end
```

```
q = vpa(q,6);

for z = 1:4,
   before_w3(z) = q(z)*U3(z);
end
w3 = sum(before_w3);

Kx = vpa(diff(w3,x,2),6);
Ky = vpa(diff(w3,y,2),6);
%K = Kx + Ky;
%Kavg = vpa(1/(a*b)*int(int(K,x,0,a),y,0,b),6);
Kavg = vpa(1/a*int(Kx,x,0,a),6);
tau = 3:.0001:3.3;
Moment = Dstiff*b*Kavg;

width = b;
g31 = -9.5e-3;
Epiezo = 62e9;
psi = (Estiff*thickAL)/(Epiezo*thickPZT);
Vpinforce_sym = (6*g31)/(width*thickAL*(3-psi)).*Moment;
Vpinforce = subs(Vpinforce_sym,'t',tau2);
T = thickAL/thickPZT;
Venhanced_sym = (6*g31*T)/(width*thickPZT*(3*T^2-1-psi*T^2)).*Moment;
Venhanced = subs(Venhanced_sym,'t',tau2);
Veb_sym =
(6*g31*psi*(1+T))/(width*thickPZT*(1+psi^2*T^2+2*psi*(2+3*T+2*T^2))).*Moment;
Veb = subs(Veb_sym,'t',tau2);

Rsource = 3900;
Ppinforce_i = [];
Penhanced_i = [];
Peb_i = [];
Rload = 100:100:1e5;
for RL = 100:100:1e5
   Ppinforce = (mean(Vpinforce.^2)*(RL/(RL+Rsource)^2));   %the root part of RMS
cancels out with the subsequent ^2 term when calc'ing power = V^2/R
   Penhanced = (mean(Venhanced.^2)*(RL/(RL+Rsource)^2));
   Peb = (mean(Veb.^2)*(RL/(RL+Rsource)^2));

   Ppinforce_i = [Ppinforce_i Ppinforce];
   Penhanced_i = [Penhanced_i Penhanced];
   Peb_i = [Peb_i Peb];
end

Power_pinforce = max(Ppinforce_i)
Power_Penhanced = max(Penhanced_i)
```

```
Power_Peb = max(Peb_i)
```

Random Noise input analytical model for plate

Mathematica

$$\text{Do}\Big[\text{qR}[z][t\_] = \text{Chop}\Big[\frac{1}{\omega\text{damp}[z]} * e^{-\zeta*\omega n[z]*t} * \frac{1}{\text{m1}} * \text{U3ab}[z] * \sum_{\omega=1}^{50}\int_0^t (.4*\text{Sin}[\text{Random}[\text{Real}, \{1, 1000\}]*2*\pi*\text{tt} - \text{Random}[\text{Real}, \{0, 2*\pi\}]]) * e^{\zeta*\omega n[z]*\text{tt}} * \text{Sin}[\omega\text{damp}[z]*(t-\text{tt})]\, d\text{tt}\Big], \{z, 1, 5\}\Big];$$

$$\text{Do}[\text{U3curv}[z][x\_, y\_] = \partial_{x,x}\text{U3}[z][x, y], \{z, 1, 5\}];$$

$$\text{Do}\Big[\text{U3int}[z][x\_, y\_] = \frac{1}{a}\int_0^a \text{U3curv}[z][x, y]\, dx, \{z, 1, 4\}\Big];$$

$$\kappa\text{avgR}[t\_] = \sum_{z=1}^{4}\text{qR}[z][t] * \text{U3int}[z][x, y];$$

$$\text{MomentPlateR}[t\_] = \text{Chop}[-\text{Dstiff}*b*\kappa\text{avgR}[t]];$$

$$\text{VpinforceR}[t\_] = \frac{6*\text{g31}}{b*\text{thickAL}*(3-\Psi)} * \text{MomentPlateR}[t];$$

$$\text{VenhancedR}[t\_] = \frac{6*\text{g31}*\text{Tratio}}{b*\text{thickPZT}*(3*\text{Tratio}^2 - 1 - \Psi*\text{Tratio}^2)} * \text{MomentPlateR}[t];$$

$$\text{VebR}[t\_] = \frac{6*\text{g31}*\Psi*(1+\text{Tratio})}{b*\text{thickPZT}*(1+\Psi^2*\text{Tratio}^2 + 2*\Psi*(2+3*\text{Tratio}+2*\text{Tratio}^2))} * \text{MomentPlateR}[t];$$

$$\text{RLoad} = 3900;$$

$$\text{PpinforceR} = \sum_{t=0}^{1000}\frac{\text{VpinforceR}[2+t*.0001]^2}{1001} * \frac{\text{RLoad}}{(\text{RLoad}+\text{Rsource})^2}$$

$$\text{PenhancedR} = \sum_{t=0}^{1000}\frac{\text{VenhancedR}[2+t*.0001]^2}{1001} * \frac{\text{RLoad}}{(\text{RLoad}+\text{Rsource})^2}$$

$$\text{PebR} = \sum_{t=0}^{1000}\frac{\text{VebR}[2+t*.0001]^2}{1001} * \frac{\text{RLoad}}{(\text{RLoad}+\text{Rsource})^2}$$

MATLAB
(all else is same as plate MATLAB code above)

```
Force_i = 0;
freqrange = 1000*2*pi;
for i = 1:50,
   Force_a = 0.4*sin(rand(1)*freqrange*tt-rand(1)*2*pi);
   Force_i = Force_i + Force_a;
end
Force = vpa(Force_i*1/m1*U3ab,6);
```

Vita

Timothy Eggborn, son of Hugh and Carol Eggborn, was born on August 23, 1979, in Richmond, Virginia. He grew up living on his family's farm in Eggbornsville, Virginia. After obtaining his Bachelor's Degree in Mechanical Engineering in 2001 at Virginia Polytechnic Institute and State University, Mr. Eggborn choose to pursue graduate studies under Dr. Daniel J. Inman at Virginia Polytechnic Institute and State University. At the Center for Intelligent Material Systems and Structures (CIMSS), he conducted his research on power harvesting with piezoelectric materials. Timothy intends to continue his work in the field of mechanical engineering in industry.